Tidally driven porewater exchange and diel cycles control CO_2 fluxes in mangroves

Alex Cabral[1*], Yvonne Y. Y. Yau[1], Gloria M. S. Reithmaier[1], Luiz Cotovicz[2], João Barreira[3], Göran Broström[1], Bárbara Viana[4], Alessandra L. Fonseca[4], Isaac R. Santos[1]

[1]Department of Marine Sciences, University of Gothenburg, Sweden
[2]Department of Marine Chemistry, Leibniz Institute for Baltic Sea Research, Germany
[3]Department of Geochemistry, Fluminense Federal University, Brazil
[4]Department of Oceanography, Federal University of Santa Catarina, Brazil
Corresponding author: Alex Cabral (alex.cabral@gu.se)

Abstract

Mangrove soils are highly enriched in organic carbon. Tidal pumping drives seawater and oxygen into mangrove sediments during flood tide and releases carbon-rich porewater during ebb tides. Here, we resolve semi-diurnal (flood/ebb tides), diel (day/night) and weekly (neap/spring tides) drivers of porewater-derived CO_2 fluxes in two mangroves and update global estimates of CO_2 emissions. Tidal pumping controlled pCO_2 variability within the mangrove creeks. The highest values of pCO_2 (2,585-6,856 µatm) and ^{222}Rn (2,315-6,159 dpm m^{-3}) and lowest values of pH (6.8-7.1) and dissolved oxygen (1.7-3.7 mg L^{-1}) at low tides were due to enhanced porewater export. ^{222}Rn and pCO_2 in mangrove porewater were respectively 4-15 and 38-41 times greater than surface waters. pCO_2 increased by 50±30% from high to low tide, 9±22% from day to night and 57±5% from neap to spring tide with clear changes on hourly, diel, and weekly time scales. Both porewater-derived CO_2 and water-air outgassing increased with tidal amplitudes ($r^2 = 0.34$, $p < 0.05$). Combining our new estimates with literature data, global porewater-derived (16 sites) and water-atmosphere (52 sites) CO_2 fluxes in mangroves would be upscale to 45±12 and 41±10 Tg C y^{-1}, respectively. These fluxes account for 25% of net primary production and 238% of sediment carbon burial rates in global mangroves. Overall, our local observations and global compilation suggest that porewater-derived CO_2 exchange is a major but often unaccounted source of CO_2 in mangroves – which can be emitted to the atmosphere or laterally exported to the ocean – and should be included in carbon budgets to solve global imbalances.

Key words: ^{222}Rn; radon mass-balance; greenhouse gases; blue carbon.

Introduction

Mangroves are highly productive ecosystems occurring in the (sub)tropical regions supporting several ecosystems services such as climate change mitigation via carbon sequestration and storage (Macreadie et al. 2021; Alongi 2022a). Mangrove forests have one of the highest organic carbon accumulation rates among all ecosystems on Earth given the high rates of primary productivity and ability to trap carbon in the anoxic sediment layers (McLeod et al. 2011; Alongi 2014). In addition, soil carbon outwelling followed by ocean storage increases the potential carbon sequestration capacity of mangroves (Sippo et al. 2016; Cabral et al. 2021; Santos et al. 2021).

Mangrove carbon returns to the atmosphere due to microbial decomposition within organic-rich sediments layers followed by water-air exchange (Kristensen et al. 2008a; Alongi 2014). Mangrove sediments are partly permeable due to irrigation by abundant crab burrows and pneumatophores which allows seawater to infiltrate into deep layers and supply electron acceptors for organic matter respiration (Xiao et al. 2021; Kristensen et al. 2022). Tidal variations in mangroves drive seawater inflow into sediments during flood tide and the discharge of porewater at ebb tides (Chen et al. 2021). This process, called tidal pumping, releases CO_2 from sediments.

CO_2 fluxes in mangroves experience substantial fluctuations due to both tidal exchange and diel effects influenced by photosynthetic organisms and respiration across day/night cycles (Maher et al. 2015; Saifullah et al. 2016). However, little is known about the relative contribution and interactions of diel (day and night), tidal (ebb and flood tides) and biweekly (neap to spring) cycles in mangrove CO_2 fluxes. Previous investigations have quantified porewater-derived (Santos et al. 2019; Chen et al. 2021) or water-atmosphere CO_2 fluxes in mangrove creeks (Taillardat et al. 2018b; Call et al. 2019a; Reithmaier et al. 2020). A combined assessment considering different time scales and global datasets is still needed to advance our understating of CO_2 drivers in mangroves.

The naturally occurring ^{222}Rn (radon, half-life 3.8 d) is an effective tracer of porewater exchange or recirculated seawater in mangroves (Gleeson et al. 2013; Tait et al. 2016). Radon has a nonreactive behavior and can be measured continuously. When coupled with trace gas analyzers, radon enables the quantification of porewater-derived CO_2 exchange rates (Santos et al. 2012). High concentrations of parent isotope ^{226}Ra is released from mangrove sediments during flood tide, also providing high ^{222}Rn activities to surface creek waters through radioactive decay and allowing the quantification of porewater exchange using comprehensive mass balance approaches (Taniguchi et al. 2019; Rodellas et al. 2021). Here, we analyzed high-resolution ^{222}Rn and CO_2 observations from two mangroves in meso- and micro-tidal regions over complete neap-spring tidal cycles to assess tidal, diel, and weekly effects on CO_2 fluxes. To put our results in perspective, we also compiled porewater-derived and water-atmosphere CO_2 fluxes across micro-, meso- and macrotidal mangroves from the literature. We then updated global estimates and uncertainties of CO_2 fluxes in mangroves.

Methods

Study sites

Field observations were performed in two mangrove tidal creeks in Brazil (Fig. 1). One mangrove creek is situated near Paraty city (Rio de Janeiro) in a tropical region, (23°18'06.2"S 44°38'53.6"W). Average monthly temperature and precipitation oscillate around 23 ± 3 °C (18 - 28 °C) and 130 ± 108 mm (0 - 501 mm), respectively. The creek catchment area (9,572 m^2) is in a pristine reserve with negligible anthropogenic impact (Chynel et al. 2022). The tidal creek catchment is part of a broader mangrove forest area of 260,112 m^2. The mangrove exchanges water with the oligotrophic Mamanguá bay and southeast Brazil shelf (Brandini et al. 2019).

The second mangrove creek is situated in the South Bay of Florianópolis city in the State of Santa Catarina (27°38'55.6"S 48°33'11.2"W, Fig. 1). The climate is subtropical with average monthly temperatures and precipitation oscillating around 21 ± 3 °C (14 - 27 °C) and 150 ± 94 mm (10 - 632 mm), respectively. The tidal creek catchment (4,046 m^2) and mangrove forest (146,065 m^2) are surrounded by moderate urbanization (Fig. 1). The mangrove exchanges with a mesotrophic bay under the influence of sewage and agricultural runoff (Brauko et al. 2020; Fonseca et al. 2021). Despite anthropogenic impacts nearby, the mangrove forest is in an environmental protected area with well-preserved mangrove vegetation.

The vegetation at both sites is dominated by *Rhizophora mangle*, *Avicennia schaueriana* and *Laguncularia racemosa*. Crab burrows are abundant and interconnected in the sediments. Both mangroves also have a mixed semidiurnal tidal pattern and no significant freshwater upstream inputs. The mangrove in Florianópolis has a clearly microtidal regime with astronomical amplitudes of around 1 m, whereas the mangrove in Paraty is situated in a lower mesotidal region with evident differences between neap/spring tidal amplitudes (Pagliosa et al. 2005; Whitfield and Elliott 2011).

Experimental approach

To capture diel, tidal, and weekly dynamics, time series stations were deployed in a small vessel moored in the mouth of both creeks from 28 October to 04 November 2021 in the mesotidal mangrove and 27 November to 04 December 2021 in the microtidal mangrove (Fig. 1). The observations captured 15 tidal cycles including extreme neap and spring tides. Sea level and current velocities were measured every 2 minutes using a ADCP (Nortek ECO) deployed in the mouth of each tidal creek. Salinity and temperature (Solinst Levelogger 5), dissolved oxygen (PME miniDOT) and pH (Onset HOBO pH logger) probes were attached to the vessel at 0.5 m depth and set to record every minute. Chlorophyll was also recorded every minute using a YSI EXO2. In the microtidal mangrove, the EXO2 stopped working towards the third day of sampling.

A submergible water pump was installed from the vessel at 0.5 m depth to continuously transport (3 L min^{-1}) surface mangrove creek water into a RAD AQUA DURRIDGE showerhead gas equilibrator. The headspace air was pumped to a Drierite® desiccant and then to an automated radon (^{222}Rn) detector (RAD7, DURRIDGE) coupled with a CO_2 trace gas analyzer (LI-COR 7810). The gas equilibrator and detectors were connected in series in a closed air loop (Santos et al. 2012). The ^{222}Rn activities (measured each 30 min) and pCO_2 (1 min frequency) in air were converted to dissolved in seawater using their partitioning and solubility coefficients (Weigel 1978; Pierrot et al. 2009). The time series data were integrated using moving averages every hour to allow comparison across the different variables and time scales.

Porewater samples (N = 24) were collected during ebb tide in both mangroves towards the end of neap (N = 12) and spring (N = 12) tidal cycles. In the mesotidal mangrove, porewater was sampled from seeping water from crab burrows, which integrates the creek sediment signature (Xiao et al. 2021). In the microtidal mangrove, bores were dug in the mud up to 50 cm depth and purged two times before sampling immediately after porewater recharging. A Solinst peristaltic pump (model 410) and 2L gas-tight polyethylene bottles were used to collect porewater samples which were analyzed using a RAD7 (Lee and Kim 2006). Salinity, temperature, oxygen, and pH in porewater were measured *in situ* with the equipment described above. Atmospheric data (temperature, wind speed and precipitation) were provided by local meteorological stations (A619 - 23°13'25.8"S 44°43'31.8"W and A806 - 27°36'09.6"S 48°37'12.3"W) from the Brazilian Institute of Meteorology (INMET, https://bdmep.inmet.gov.br/), installed in 10-m high towers and located ~10km from the study sites. Atmospheric CO_2 was retrieved from the NOAA global mean (https://gml.noaa.gov/ccgg/trends/global.html).

Water-atmosphere CO_2 fluxes calculations

The surface CO_2 fluxes (F, mmol m^2 d^{-1}) in the water-air interface were determined according to:

$$F = k\ \alpha\ \left(pCO_{2_{(water)}} - pCO_{2_{(air)}}\right) \qquad \text{Eq. 1}$$

where *k* is the gas transfer velocity (m d^{-1}), α is the CO_2 solubility coefficient (mol / (kg atm)), $pCO_{2(water)}$ and $pCO_{2(air)}$ are the CO_2 partial pressures (µatm) in the water (hourly averages) and atmosphere, respectively. Solubility coefficient for CO_2 were determined according to Weiss (1974). The *k* values were determined using four different models (Borges et al. 2004, Eq. 2; Ho et al. 2016, Eq. 3; Rosentreter et al. 2017, Eq. 4; Jeffrey et al. 2018, Eq. 5) derived from parametrizations based on wind speed (v, m s^{-1}), current velocity (u, cm s^{-1}), and depth (h, meters) for mangroves:

$$k_{600} = 1.0 + 1.719v^{0.5}h^{-0.5} + 2.58u \qquad \text{Eq. 2}$$

$$k_{600} = (0.77v^{0.5}h^{-0.5}) + (0.266u^2) \qquad \text{Eq. 3}$$

$$k_{600} = -0.08 + 0.26v + 0.59h + 0.83u \qquad \text{Eq. 4}$$

$$k_{600} = -0.175 + 0.467v + 1.28h + 0.7u \qquad \text{Eq. 5}$$

The *k* was normalized to a Schmidt number (Sc) of 600 as a function of salinity and temperature, using the equation of Wanninkhof (2014):

$$k_{600} = k\ (600/Sc)^{-0.5} \qquad \text{Eq. 6}$$

Radon (^{222}Rn) mass-balance model and porewater exchange

A radon mass balance model was used to calculated porewater exchange rates in both mangroves as previously applied in similar tidal creeks (Tait et al. 2016; Call et al. 2019a; Santos et al. 2019; Chen et al. 2021). The model accounts for different sources (inflow during flood tides, diffusion from sediments and ^{222}Rn inputs from ^{226}Ra decay) and sinks (outflow during ebb tides, ^{222}Rn radioactive decay and atmospheric evasion) of radon in the tidal creek. The porewater exchange rates (PW) were calculated as follow:

$$PW\ (m^3h^{-1}) = \frac{(Rn_wQ + J_{atm}A + Rn_w\lambda V) - (Rn_{dif}A + Ra_{dec}\lambda V)}{PW_{end}} \quad \text{Eq. 7}$$

where Rn_w (dpm m^{-3}) is the ^{222}Rn concentration in surface water, Q is the water discharge (m^3 h^{-1}), A is the mangrove inundated area (m^2), V is the water volume of the tidal creek (m^3), λ is the decay constant of ^{222}Rn (0.215 h^{-1}) and PW_{end} is the average ^{222}Rn concentration in porewater minus the concentration in surface water at each hour during the time series. Ra_{dec} is the ^{222}Rn concentration produced through ^{226}Ra decay (dpm m^{-3}), radium was analyzed by filtering surface water through MnO_2 impregnated fibers which were analyzed for ^{226}Ra via delayed coincidence counter (RaDeCC) (Diego-Feliu et al. 2020). J_{atm} (dpm m^{-2} h^{-1}) is the atmospheric evasion of ^{222}Rn due to wind, currents, and depth. ^{222}Rn water-air transfer velocities (*k*) were calculated using the parametrization on equations 2-5 and normalized to the Schmidt number (Eq. 6) at *in situ* temperature and salinity (Wanninkhof 2014). The average flux between the 4 models were used to estimated J_{atm}:

$$J_{atm} = k(Rn_w - \alpha Rn_{atm}) \quad \text{Eq. 8}$$

where *k* is the ^{222}Rn transfer velocity (cm h^{-1}), Rn_{atm} is the average ^{222}Rn concentration (dpm m^{-3}) in the atmosphere and α is the Oswald solubility coefficient. Since ^{222}Rn atmospheric evasion can represent a major sink of radon in mangroves and modify porewater exchange rates (Chen et al. 2021), we calculated two J_{atm} and sum them: one J_{atm} for the mangrove creek main channel during the whole time series and another for when the mangrove forest is flooded. This prevents overestimation of ^{222}Rn evasion when upscaling by the hourly mangrove catchment area due to the overlaying water at high tide where we assumed the influence of wind and currents is zero because of friction with soil and tree density cover.

The approach provides more conservative estimates of k, down to 11 ± 4 times lower in the inundated forest when compared to the gas transfer velocities in the main creek channel. Rn_{dif} (dpm m^{-2} h^{-1}) is the radon diffusion from sediments, calculated using a depth-independent approach (Corbett et al. 1998):

$$Rn_{dif} = (\lambda D_s)^{0.5}(PW_{end}) \quad \text{Eq. 9}$$

where D_s is effective wet bulk sediment diffusion (m^2 h^{-1}) coefficient calculated as a function of water temperature and sediment porosity (0.85 and 0.50 for sediments in the mesotidal and microtidal mangrove, respectively). The hourly porewater exchange fluxes were integrated over full daily tidal cycles (m^3 d^{-1}) and normalized by the total catchment area of each mangrove to estimated porewater exchange rates (cm d^{-1}). The porewater-derived CO_2 fluxes (mmol h^{-1}) were assessed by multiplying the porewater exchange rates (m^3 h^{-1}) by the average CO_2 concentration (mmol m^{-3}) in porewater samples minus the CO_2 in surface waters at each hour, which were then integrated over full daily tidal cycles and normalized by the mangrove catchment areas (mmol m^2 d^{-1}).

Results

Surface water time-series

Water depths were similar in both mangrove tidal creeks, 1.9 ± 0.3 m for the microtidal and 1.6 ± 0.4 m for the mesotidal (Tab. 1). However, as expected, neap and spring tidal amplitudes were greater in the mesotidal (0.9 - 1.8 m) than the microtidal (0.4 - 0.9 m). Current velocities and wind speeds were also similar in both creeks, 28.6 ± 18.2 and 31.8 ± 12.8 cm s^{-1} and 1.9 ± 1.2 and 1.2 ± 0.9 m s^{-1} for the micro- and mesotidal creeks, respectively. Water temperature was higher in the microtidal (25.3 ± 1.2 °C) than mesotidal (22.7 ± 0.5 °C) mangrove, also showing higher variation in the microtidal (Tab. 1). Water temperature was controlled by diel variations in both sites, whereas salinity had more influence of tidal variation, especially in the mesotidal mangrove towards the spring tide (Fig. 2 & 3).

Lowest values of salinity were found in the mesotidal site under effect of precipitation. Accumulated rainfall during the time series was around ten times higher in the mesotidal mangrove (57.8 mm) than the microtidal (5.6 mm), decreasing salinity to 23.1 (Tab. 1). We found similar salinity in surface (31.6 ± 1.2) and porewater (31.4 ± 0.7) in the microtidal system. Much lower salinity (24.4 ± 2.6) was found in the mesotidal mangrove porewater, closer to the lowest salinity values found in this mangrove surface water time series (Fig. 3). Dissolved oxygen (DO) values were similar at the two sites (Tab. 1). The DO variability followed diel cycles in the microtidal site and tidal cycles in the mesotidal mangrove (Fig. 2 & 3). Stronger positive correlations between oxygen and depth in the mesotidal ($r^2 = 0.30$, $p < 0.001$) than the microtidal ($r^2 = 0.11$, $p < 0.001$) imply a shift in the time scales of oxygen cycles (Fig. 4). Chlorophyll observations showed contrasting patterns between mangroves. Whereas high chlorophyll was observed in the low tides in the microtidal mangrove, the mesotidal showed the highest concentration during high tides (Fig. 2 & 3). Overall, more chlorophyll was found in the mesotidal (6.1 ± 2.5 µg L^{-1}) than microtidal (3.9 ± 2.4 µg L^{-1}) mangrove.

pH patterns mimicked DO with positive correlations with depth and higher values of pH during high tide (Fig. 4). A diel cycle was also observed for pH in both sites with higher pH during the day than night (Fig. 2 & 3). The pCO_2 was 3 times higher in the microtidal (2403.9 ± 1545.0 µatm) than the mesotidal (893.2 ± 357.0 µatm) mangrove. In both systems, high pCO_2 was associated with low pH and oxygen values (Fig. 5). However, pCO_2 showed contrasting trends with salinity at the two sites. High pCO_2 occurred at high salinity in the microtidal mangrove and low salinity in the mesotidal (Fig. 5). ^{222}Rn generally showed a tidal pattern with higher activities during low than high tides (Fig. 2, 3 & 4).

Mangrove porewater observations

Porewater pCO_2 and ^{222}Rn showed considerable variability, ranging from 2468 to 278766 µatm and 2780 to 40322 dpm m^{-3}. pCO_2 in porewater was 41 and 38 times higher than average surface water values in the microtidal and mesotidal mangrove, respectively (Tab. 1 & 2). ^{222}Rn also showed elevated concentrations in porewater, up to 4-15 times higher than surface waters (Fig. 6).

Mangrove water-atmosphere CO_2 fluxes

Both mangroves were a net source of CO_2 to the atmosphere. The CO_2 fluxes and gas transfer velocities were different when using different models' parametrizations in neap and spring tides (Tab. 3). Overall, water-air CO_2 fluxes in the microtidal mangrove (142.9 ± 140.7 mmol m^{-2} d^{-1}) were ~4 times higher than the mesotidal (38.4 ± 30.7 mmol m^{-2} d^{-1}). These differences between mangroves were higher in the spring (x 4.2) than neap (x 3.4) tides (Tab. 3). Within each mangrove forest, water-air CO_2 fluxes were 2 and 3 times higher in the spring than neap tides for the meso- and microtidal observations, respectively.

Although CO_2 fluxes were variable across mangroves and tidal cycles, average gas transfers velocities (k, m d^{-1}) were similar in both systems using all data (2.4 - 2.6) and during neap (2.0 - 2.4) and spring (3.0 - 3.1) tides. Weak correlations ($r^2 < 0.20$) were found between transfer velocities and CO_2 fluxes, both for the 4 individual models separated and average results. However, strong correlations ($p < 0.01$) between pCO_2 and CO_2 fluxes in both the microtidal ($r^2 = 0.88$, N = 170) and mesotidal ($r^2 = 0.68$, N = 184) mangroves were observed. Across models, average CO_2 fluxes oscillated from 14.9 ± 14.0 to 59.5 ± 43.1 mmol m^{-2} d^{-1} in the mesotidal mangrove and 53± 50.6 to 225.9 ± 237.3 mmol m^{-2} d^{-1} in the microtidal.

We used four empirical models based on depth, currents velocity and wind speed to derive gas transfer velocities and estimate water-air CO_2 fluxes in the creek. The equations from Borges et al. (2003) and Rosentreter et al. (2017) showed median values whereas the lowest and highest gas transfer velocities (k) were obtained using the parametrizations by Ho et al. (2016) and Jeffrey et al. (2018), respectively. We used an average of all models and associated uncertainties to allow direct comparations with previous studies in mangroves and provide a range of potential CO_2 outgassing.

Radon mass balance and porewater-derived CO_2 exchange

Porewater exchange and atmospheric evasion were the main sources and sinks in the radon mass balance model, corresponding to 47% and 44% of the fluxes in the microtidal creek and 50% and 40% in the mesotidal, respectively (Tab. 4). The other fluxes included in the model were minor components accounting for ~10% of the total ^{222}Rn budget. Porewater exchange rates were estimated to be 2.7 ± 2.3 and 27.8 ± 10.2 10^3 m^3 d^{-1} for the micro- and mesotidal mangroves, respectively (Tab. 4). Considering the mangrove intertidal areas, porewater exchange would convert to 1.8 ± 1.6 and 10.7 ± 3.9 cm d^{-1}, respectively. Uncertainties represent the natural variability over the 15 tidal cycles investigated at each site.

CO_2 concentrations in porewater oscillated between 77.3 – 8351.0 µM (equivalent to 2.5 – 278.8 10^3 µatm) in the mesotidal mangrove and 882.8 – 2538.3 µM (equivalent to 27.6 – 84.8 10^3 µatm) in the microtidal. Using CO_2 porewater average concentration minus the mangrove surface water concentrations as endmembers, porewater-derived CO_2 discharge would convert to 35.5 ± 22.5 and 110.4 ± 40.2 mmol m^{-2} d^{-1} for the micro- and mesotidal mangroves, respectively (Tab. 4). Given that porewater exchange is driven by the tides, we found that both porewater exchange ($r^2 = 0.39$, $p < 0.05$) and porewater-derived CO_2 fluxes ($r^2 = 0.29$, $p < 0.05$) increased as tidal amplitude increased during the neap-spring tidal cycles (Fig. 8).

Discussion

Tidal pumping as a driver of porewater exchange

Our observations in a tropical mesotidal and subtropical microtidal mangrove demonstrated substantial temporal and spatial variability across tidal, diel, and neap-spring scales. Changing hydrostatic pressure gradients during flood and ebb tides are the main drivers of porewater exchange between the mangrove sediments and surface waters (Chen et al. 2021). The tides oscillate according astronomical and meteorological patterns, proximity with the open ocean and bathymetry, influencing the magnitude of tidal amplitudes and carbon fluxes in intertidal systems (Lyard et al. 2006). The ^{222}Rn mass balance models demonstrated that the exchange of mangrove porewater with the tidal creek varied substantially during the time series and that it increases with tidal amplitude over neap-spring tidal cycles (Fig. 8). Porewater exchange rates increased significantly with tidal range from 3.3 ± 2.1 cm d^{-1} in the microtidal mangrove to 27.8 ± 10.2 cm d^{-1} in the mesotidal creek. This was also observed in mangroves in Australia (Chen et al. 2021) and Vietnam (Taillardat et al. 2018b) when using ^{222}Rn to trace porewater exchange over tidal cycles. Most studies tracing porewater in mangroves have less than 2 days of continuous ^{222}Rn observations (Tab. A1), which limit comparison among sites and the detection of variations across cycles giving the high dynamic nature of mangroves. Latitudinal cross-comparation of porewater exchange rates in Australian mangroves showed significant relationships with tidal amplitude only for a few systems (Tait et al. 2016).

Our compilation of studies across different mangroves showed that there is no clear relationship between tidal amplitudes and porewater exchange over large scale (Tab. A1) perhaps due to the short-term nature of most datasets. Although the largest tidal amplitudes occur in the equatorial macrotidal mangroves, the highest porewater exchange was observed in mesotidal systems (12.3 ± 11.3 cm d^{-1}). High uncertainties are related to the limited porewater exchange data in mangroves, especially in macrotidal systems and within tidal creeks surrounded by developed mangrove forests without the influence of freshwater sources. Efforts to expand research in global mangrove hotspots of Asia, Latin America and Africa will refine estimates and reduce uncertainties.

Upscaling the average porewater exchange rates for micro-, meso- and macrotidal mangroves (Tab. A1) by their global areas (Giri et al. 2011) resulted in a tidally derived global mangrove porewater discharge of 4,639 ± 3,777 Km^3 $year^{-1}$. This represents 14 ± 11 to 20 ± 17 times the global volume of fresh groundwater discharge (Luijendijk et al. 2020) or 12 ± 10 % of the global river discharge (Fekete et al. 2002) to the ocean. Our results suggest that although mangroves only cover 12-15% of Earth's coastlines they effectively recirculate seawater within their permeable sediments on diel and biweekly time scales, releasing carbon from soils during tidal pumping.

Porewater-derived versus water-atmosphere CO_2 fluxes

Mangroves can release greenhouse gases to the atmosphere and contribute to both local and global carbon budgets (Call et al. 2019b; Alongi 2022b; Lu et al. 2023). However, most of literature in mangroves has focused on quantifying water-air and soil-air CO_2 fluxes (Borges et al. 2003; Kristensen et al. 2008b; Rosentreter et al. 2018) while overlooking CO_2 porewater exchange. The few studies continuously capturing high resolution radon and CO_2 measurements demonstrated that porewater exchange is the major CO_2 source in surface water of mangrove creeks (Taillardat et al. 2018a; Call et al. 2019a; Santos et al. 2019; Chen et al. 2021). Our high frequency datasets support this suggestion. Positive correlations between tidal amplitudes over neap-spring cycles and porewater-derived CO_2 fluxes imply that tidal pumping was the major source of CO_2 outgassing in mangrove tidal creeks.

Other drivers such as rainfall and anthropogenic impacts might influence pCO_2 dynamics and fluxes. Rainfall in the mesotidal, pristine mangrove decreased ($p < 0.05$) both pCO_2 ($r^2 = 0.57$) and water-air CO_2 fluxes ($r^2 = 0.64$) in the tidal creek. Pulses of precipitation dilute CO_2 concentrations in pore- and surface waters, as observed in mangroves in Australia (Call et al. 2015; Chen et al. 2021), since pCO_2 in rain is likely to be in equilibrium with atmosphere (~ 424 ppm, NOAA). Observations in Vietnam mangroves found higher CO_2 fluxes in the monsoon rather than dry season (Vinh et al. 2019) due to upstream riverine inputs. This pCO_2 increase during wet conditions is not observed in the mesotidal mangrove due to absence of upstream river CO_2 inputs.

Higher urbanization and eutrophic settings surrounding the microtidal mangrove (Cabral et al. 2020) compared to the pristine, mesotidal creek (Chynel et al. 2022) also contribute to organic enrichment and increase pCO_2 in the microtidal creek. Previous studies found that sediment-atmosphere CO_2 fluxes were 3 times lower in the mesotidal creek (~120 mmol m^{-2} d^{-1}) when compared to a nearby eutrophic mangrove (Barroso et al. 2022), confirming that pristine mangroves emit less CO_2 into the atmosphere than impacted/eutrophic systems. The dry soil-air flux found by Barroso et al. (2022) is much higher than the average water-air CO_2 emission (38 ± 31 mmol m^{-2} d^{-1}) found by our study but comparable to the CO_2 porewater-exchange rates in that system (110 ± 40 mmol m^{-2} d^{-1}) or to the global average for mesotidal mangroves (92 ± 84 mmol m^{-2} d^{-1}, Table 5).

Diel cycles played a secondary role driving most of variables analyzed in both mangrove creeks (Fig. 7). Stronger diel effects were observed in the microtidal mangrove for pCO_2, DO and chlorophyll where 22 ± 19%, 45 ± 18% and 24 ± 4% of the variation was explained by day/night differences, respectively. Phytoplankton primary production can lower pCO_2 during the day in mangrove creeks, decreasing CO_2 outgassing to the atmosphere (Zablocki et al. 2011; Maher et al. 2015; Cotovicz et al. 2020). Contrasting patterns during chlorophyll time series showed biomass peaks during high and low tides for the mesotidal and microtidal mangrove, respectively, indicating autochthonous phytoplankton production for the microtidal and supporting the stronger diurnal control on that creek.

We found opposite patterns of CO_2 water-air and porewater fluxes between the micro- and mesotidal mangroves due to the differences in pCO_2 and tidal ranges, respectively (Tab. 4). When combining CO_2 water-air and porewater fluxes, total CO_2 flux would be similar in both mangroves due to the elevated pCO_2 in the microtidal mangrove and higher tidal pumping in the mesotidal site. Water-air CO_2 strongly correlated ($r^2 = 0.74$) with pCO_2 but no significant correlations were found with the gas transfer velocities (k). This indicates that water-air CO_2 fluxes were mostly a function of pCO_2 enrichments driven by tidal pumping rather than removal driven by turbulence.

We found different trends related to tidal pumping when combining both mangroves tidal cycles and CO_2 outgassing fluxes. The higher water-atmosphere CO_2 fluxes found in the microtidal creek compared to the mesotidal were related to the higher pCO_2 in both pore- and surface water. When analyzing the tidal cycles in both creeks separately, we found positive correlation between tidal ranges and CO_2 outgassing as also observed in Amazon mangroves (Call et al. 2019b). Water-air CO_2 fluxes from neap to spring tides increased 38% and 40% in the mesotidal and microtidal creeks, respectively. Longer inundation time of mangrove sediment during spring tides lead to peaks of CO_2 emissions when compared to neap tides when porewater exchange is mostly constrained by the creek sediment banks. Our results indicate that overlooked temporal variability over neap-spring tidal cycles might biased estimates built on spatial surveys or only few days of measurements. Hence, our new observations build on previous work in mangroves (Call et al. 2015; Sadat-Noori et al. 2016) and saltmarshes (Chen et al. 2022; Correa et al. 2022) highlighting the dominating role played by semi-diurnal and biweekly tidal cycles.

Implications to mangrove global CO_2 fluxes

The global mangrove carbon budget has been conceptualized to illustrate the multiple carbon pathways and sequestration capacity by mangrove soil and outwellling as blue carbon (Alongi 2020, 2022b). The key terms of the carbon budget in mangroves are CO_2 exchange by primary producers (mangrove trees and algae), water-air and sediment-air emissions, carbon burial in sediments and outwelling to the ocean. Our results and recent studies (Tait et al. 2016; Taillardat et al. 2018a; Call et al. 2019a; Chen et al. 2021) show evidence that porewater exchange by tidal pumping is a major CO_2 pathway in mangroves. We use our new datasets and earlier observations to estimate the contribution of porewater as a source of CO_2 as well as update global estimates of CO_2 water-air exchange.

Global porewater-derived CO_2 exchange in mangroves was estimated to be 45.4 ± 11.7 Tg C y^{-1} (Tab. 5). Our global compilation excluded sites with large freshwater or upstream riverine CO_2 sources in the mangrove tidal creek that would create biases in the interpretation. Large uncertainties (85.9 ± 73.2 mmol m^{-2} d^{-1}) on CO_2 porewater fluxes are associated with high spatial variability and lack of data in many regions, especially in macrotidal tropical mangroves (Tab. A1). Our upscaled porewater-derived CO_2 flux represents ~25% of the global mangrove net primary production (Alongi 2020) or about 238% of mangrove soil carbon burial rates (Breithaupt and Steinmuller 2022) (Fig. 9).

The global dataset of CO_2 outgassing spans a larger latitudinal and tidal range when compared to porewater-deliver CO_2 exchange (Tab. A1 and A2). Most research assessing water-air CO_2 fluxes are concentrated in micro- (38%, N = 19 sites) or mesotidal (40%, N = 20) mangrove systems. Just a few studies made observations in different seasons or over neap-spring cycles using high-frequency datasets. Our updated global water-air CO_2 fluxes resulted in average mangrove CO_2 emissions of 40.9 ± 10.3 Tg C y^{-1}. This is ~15% higher than reported by Rosentreter et al. (2018) (34.1 ± 5.4 Tg C y^{-1}) but ~10% lower than the latest published global compilation by Call et al. (2019b) of 45.5 Tg C y^{-1}. All studies used the same mangrove area of 137759 Km^2 (Giri et al. 2011) to allow direct comparison. The similar porewater-derived and water-air global CO_2 emissions found by our study highlights that most CO_2 is released to the atmosphere as soon as porewater discharges to surface waters due to the short residence times and high pCO_2 gradients at the water-air interface. Major differences when contrasting with the latest review (Call et al. 2019b) are related to lower CO_2 emissions (-5 Tg C y^{-1}) in mesotidal mangroves where more than half of all mangrove forests are located. Macrotidal mangroves are still underrepresented with only 23% of water-air CO_2 fluxes studies covering this tidal range and mostly concentrated in India and Australia. Despite these limitations, this study is the first attempt to synthesize both water-air and porewater-exchange CO_2 fluxes in mangroves at a global scale. Even with growing datasets, no significant trends emerged between tidal ranges and CO_2 fluxes using all data available. This lack of correlation is probable related to CO_2 observations in different seasons (dry vs. wet), geomorphic (e.g. lagoonal or open coast) and sedimentary (terrigenous or carbonate) settings, sampling design (spatial survey vs. time series observations) and resolution (hourly/daily discrete or continuous over neap-spring cycles), anthropogenic impacts, and/or the use of different methods to estimate CO_2 outgassing (chambers/gas exchangers and several gas transfer velocity parametrization models) or porewater fluxes (usually estimated using radon or radium isotopes).

Conclusions

Porewater-derived CO_2 is a major but often unaccounted source of carbon to the water and eventually the atmosphere in mangroves. Neglecting this pathway can likely underestimate CO_2 emissions or overestimate blue carbon sequestration capacity in mangroves. Tidal pumping on a semi-diurnal (high/low tides) time scale explained half (50 ± 30%) of pCO_2 variation in the creeks, diel (day/night cycles) explained 9 ± 22% of the deviation and spring-neap cycles accounted for 57 ± 5% of the variability. Studies focusing on water-atmosphere CO_2 outgassing in mangrove tidal creeks have advanced faster than the quantification of porewater exchange. Our observations covering semi-diurnal, daily, and neap-spring cycles suggest that tidal pumping is a key mechanism enhancing CO_2 fluxes. Combining our new observations with earlier datasets results in an updated global estimate of 40.9 ± 10.3 Tg C y^{-1} for water-air CO_2 fluxes from mangroves and 45.4 ± 11.7 Tg C y^{-1} for porewater-derived CO_2 fluxes. More site-specific studies combining CO_2 and porewater tracers (e.g., ^{222}Rn) and using high-resolution time series covering multiple tidal cycles are required to refine global budgets unbalances and better understand the drives of carbon cycling in mangrove systems.

CRediT authorship contribution statement

AC wrote the manuscript, performed data analyses, and made all the figures. AC and IRS designed the project. AC, GMSR, YYYY, LC, JB, BV, ALF, and IRS performed field investigations. GB contributed with ADCP data. IRS supervised the project and obtained funding. All authors revised and approved the final version of the manuscript.

Acknowledgements

Funding was provided by the Swedish Research Council (2019-03930 and 2020-00457). We thank all who support this project, especially to Juliana Hayden, Kalina Brauko, Nilva Brandini, Natasha Costa, Luanna Azevedo, Vítor Pereira, Daniela Zanetti, Wilson Machado, and Paulo Horta.

Appendix A. Supplementary Material

Table A1 shows a global data compilation of porewater exchange rates, pCO_2 in porewater and porewater-derived CO_2 exchange in mangroves. Table A2 provide tidal amplitude, water pCO_2 (range) and average water-atmosphere CO_2 flux from this study and previously published data in 50 mangrove systems worldwide.

References

Alongi, D. M. 2014. Carbon cycling and storage in mangrove forests. Ann Rev Mar Sci **6**: 195–219. doi:10.1146/annurev-marine-010213-135020

Alongi, D. M. 2020. Carbon balance in salt marsh and mangrove ecosystems: A global synthesis. J Mar Sci Eng **8**: 1–21. doi:10.3390/jmse8100767

Alongi, D. M. 2022a. Impacts of Climate Change on Blue Carbon Stocks and Fluxes in Mangrove Forests. Forests **13**: 149. doi:10.3390/f13020149

Alongi, D. M. 2022b. Lateral Export and Sources of Subsurface Dissolved Carbon and Alkalinity in Mangroves: Revising the Blue Carbon Budget. J Mar Sci Eng **10**. doi:10.3390/jmse10121916

Barroso, G. C., G. Abril, W. Machado, and others. 2022. Linking eutrophication to carbon dioxide and methane emissions from exposed mangrove soils along an urban gradient. Science of the Total Environment **850**. doi:10.1016/j.scitotenv.2022.157988

Borges, A. V., S. Djenidi, G. Lacroix, J. Théate, B. Delille, and M. Frankignoulle. 2003. Atmospheric CO2 flux from mangrove surrounding waters. Geophys Res Lett **30**. doi:10.1029/2003GL017143

Borges, A. V., J.-P. Vanderborght, L.-S. Schiettecatte, F. Gazeau, S. Ferrón-Smith, B. Delille, and M. Frankignoulle. 2004. Variability of the gas transfer velocity of CO2 in a macrotidal estuary (the Scheldt). Estuaries **27**: 593–603. doi:10.1007/BF02907647

Brandini, F., L. S. Michelazzo, G. R. Freitas, G. Campos, M. Chuqui, and L. Jovane. 2019. Carbon Flow for Plankton Metabolism of Saco do Mamanguá Ría, Bay of Ilha Grande, a Subtropical Coastal Environment in the South Brazil Bight. Front Mar Sci **6**: 1–14. doi:10.3389/fmars.2019.00584

Brauko, K. M., A. Cabral, N. V. Costa, and others. 2020. Marine Heatwaves, Sewage and Eutrophication Combine to Trigger Deoxygenation and Biodiversity Loss: A SW Atlantic Case Study. Front Mar Sci **7**: 1–11. doi:10.3389/fmars.2020.590258

Breithaupt, J. L., and H. E. Steinmuller. 2022. Refining the Global Estimate of Mangrove Carbon Burial Rates Using Sedimentary and Geomorphic Settings. Geophys Res Lett **49**. doi:10.1029/2022GL100177

Cabral, A., C. H. C. Bonetti, L. H. P. Garbossa, J. Pereira-Filho, K. Besen, and A. L. Fonseca. 2020. Water masses seasonality and meteorological patterns drive the biogeochemical processes of a subtropical and urbanized watershed-bay-shelf continuum. Science of The Total Environment **749**: 141553. doi:10.1016/j.scitotenv.2020.141553

Cabral, A., T. Dittmar, M. Call, and others. 2021. Carbon and alkalinity outwelling across the groundwater-creek-shelf continuum off Amazonian mangroves. Limnol Oceanogr Lett **6**: 369–378. doi:10.1002/lol2.10210

Call, M., D. T. Maher, I. R. Santos, and others. 2015. Spatial and temporal variability of carbon dioxide and methane fluxes over semi-diurnal and spring-neap-spring timescales in a mangrove creek. Geochim Cosmochim Acta **150**: 211–225. doi:10.1016/j.gca.2014.11.023

Call, M., C. J. Sanders, P. A. Macklin, I. R. Santos, and D. T. Maher. 2019a. Carbon outwelling and emissions from two contrasting mangrove creeks during the monsoon storm season in Palau, Micronesia. Estuar Coast Shelf Sci **218**: 340–348. doi:10.1016/j.ecss.2019.01.002

Call, M., I. R. Santos, T. Dittmar, C. E. de Rezende, N. E. Asp, and D. T. Maher. 2019b. High pore-water derived CO 2 and CH 4 emissions from a macro-tidal mangrove creek in the Amazon region. Geochim Cosmochim Acta **247**: 106–120. doi:10.1016/j.gca.2018.12.029

Chen, X., I. R. Santos, M. Call, and others. 2021. The mangrove CO2 pump: Tidally driven pore-water exchange. Limnol Oceanogr **66**: 1563–1577. doi:10.1002/lno.11704

Chen, X., P. Zhu, Y. Zhang, and L. Li. 2022. Plum rain enhances porewater greenhouse gas fluxes and weakens the acidification buffering potential in saltmarshes. J Hydrol (Amst) 128686. doi:10.1016/j.jhydrol.2022.128686

Chynel, M., S. Rockomanovic, G. Abril, and others. 2022. Contrasting organic matter composition in pristine and eutrophicated mangroves revealed by fatty acids and stable isotopes (Rio de Janeiro, Brazil). Estuar Coast Shelf Sci **277**. doi:10.1016/j.ecss.2022.108061

Corbett, D. R., + W C Burnett, P. H. Cable, and S. B. Clark. 1998. A multiple approach to the determination of radon fluxes from sediments.

Correa, R. E., K. Xiao, S. R. Conrad, P. D. Wadnerkar, A. M. Wilson, C. J. Sanders, and I. R. Santos. 2022. Groundwater Carbon Exports Exceed Sediment Carbon Burial in a Salt Marsh. Estuaries and Coasts **45**: 1545–1561. doi:10.1007/s12237-021-01021-1

Cotovicz, L. C., L. O. Vidal, C. E. de Rezende, and others. 2020. Carbon dioxide sources and sinks in the delta of the Paraíba do Sul River (Southeastern Brazil) modulated by carbonate thermodynamics, gas exchange and ecosystem metabolism during estuarine mixin. Mar Chem **226**: 103869. doi:10.1016/j.marchem.2020.103869

Diego-Feliu, M., V. Rodellas, A. Alorda-Kleinglass, and others. 2020. Guidelines and Limits for the Quantification of Ra Isotopes and Related Radionuclides With the Radium Delayed Coincidence Counter (RaDeCC). J Geophys Res Oceans **125**. doi:10.1029/2019JC015544

Fekete, B. M., C. J. Vörösmarty, and W. Grabs. 2002. High-resolution fields of global runoff combining observed river discharge and simulated water balances. Global Biogeochem Cycles **16**: 15-1-15–10. doi:10.1029/1999gb001254

Fonseca, A. L., A. Newton, and A. Cabral. 2021. Local and meso-scale pressures in the eutrophication process of a coastal subtropical system: Challenges for effective management. Estuar Coast Shelf Sci **250**: 107109. doi:10.1016/j.ecss.2020.107109

Giri, C., E. Ochieng, L. L. Tieszen, Z. Zhu, A. Singh, T. Loveland, J. Masek, and N. Duke. 2011. Status and distribution of mangrove forests of the world using earth observation satellite data. Global Ecology and Biogeography **20**: 154–159. doi:10.1111/j.1466-8238.2010.00584.x

Gleeson, J., I. R. Santos, D. T. Maher, and L. Golsby-Smith. 2013. Groundwater-surface water exchange in a mangrove tidal creek: Evidence from natural geochemical tracers and implications for nutrient budgets. Mar Chem **156**: 27–37. doi:10.1016/j.marchem.2013.02.001

Ho, D. T., N. Coffineau, B. Hickman, N. Chow, T. Koffman, and P. Schlosser. 2016. Influence of current velocity and wind speed on air-water gas exchange in a mangrove estuary. Geophys Res Lett **43**: 3813–3821. doi:10.1002/2016GL068727

Jeffrey, L. C., D. T. Maher, I. R. Santos, M. Call, M. J. Reading, C. Holloway, and D. R. Tait. 2018. The spatial and temporal drivers of pCO2, pCH4 and gas transfer velocity within a subtropical estuary. Estuar Coast Shelf Sci **208**: 83–95. doi:10.1016/j.ecss.2018.04.022

Kristensen, E., S. Bouillon, T. Dittmar, and C. Marchand. 2008a. Organic carbon dynamics in mangrove ecosystems: A review. Aquat Bot **89**: 201–219. doi:10.1016/j.aquabot.2007.12.005

Kristensen, E., M. R. Flindt, S. Ulomi, A. V. Borges, G. Abril, and S. Bouillon. 2008b. Emission of CO2 and CH4 to the atmosphere by sediments and open waters in two Tanzanian mangrove forests. Mar Ecol Prog Ser **370**: 53–67. doi:10.3354/meps07642

Kristensen, E., T. Valdemarsen, P. Moraes, A. Güth, P. Sumida, and C. Quintana. 2022. Pneumatophores and crab burrows increase CO2 and CH4 emission from sediments in two Brazilian fringe mangrove forests. Mar Ecol Prog Ser **698**: 29–39. doi:10.3354/meps14153

Lee, J. M., and G. Kim. 2006. A simple and rapid method for analyzing radon in coastal and ground waters using a radon-in-air monitor. J Environ Radioact **89**: 219–228. doi:10.1016/j.jenvrad.2006.05.006

Lu, Z., F. Wang, K. Xiao, Y. Wang, Q. Yu, P. Cheng, and N. Chen. 2023. Carbon dynamics and greenhouse gas outgassing in an estuarine mangrove wetland with high input of riverine nitrogen. Biogeochemistry **162**: 221–235. doi:10.1007/s10533-022-00999-5

Luijendijk, E., T. Gleeson, and N. Moosdorf. 2020. Fresh groundwater discharge insignificant for the world's oceans but important for coastal ecosystems. Nat Commun **11**. doi:10.1038/s41467-020-15064-8

Lyard, F., F. Lefevre, and T. Letellier. 2006. Modelling the global ocean tides : modern insights from FES2004. 394–415. doi:10.1007/s10236-006-0086-x

Macreadie, P. I., M. D. P. Costa, T. B. Atwood, and others. 2021. Blue carbon as a natural climate solution. Nat Rev Earth Environ **2**: 826–839. doi:10.1038/s43017-021-00224-1

Maher, D. T., K. Cowley, I. R. Santos, P. Macklin, and B. D. Eyre. 2015. Methane and carbon dioxide dynamics in a subtropical estuary over a diel cycle: Insights from automated in situ radioactive and stable isotope measurements. Mar Chem **168**: 69–79. doi:10.1016/j.marchem.2014.10.017

McLeod, E., G. L. Chmura, S. Bouillon, and others. 2011. A blueprint for blue carbon: Toward an improved understanding of the role of vegetated coastal habitats in sequestering CO2. Front Ecol Environ **9**: 552–560. doi:10.1890/110004

Pagliosa, P. R., A. Fonseca, G. E. Bosquilha, and others. 2005. Phosphorus dynamics in water and sediments in urbanized and non-urbanized rivers in Southern Brazil. Mar Pollut Bull **50**: 965–974. doi:10.1016/j.marpolbul.2005.04.005

Pierrot, D., C. Neill, K. Sullivan, and others. 2009. Recommendations for autonomous underway pCO2 measuring systems and data-reduction routines. Deep Sea Res 2 Top Stud Oceanogr **56**: 512–522. doi:10.1016/j.dsr2.2008.12.005

Reithmaier, G. M. S., D. T. Ho, S. G. Johnston, and D. T. Maher. 2020. Mangroves as a Source of Greenhouse Gases to the Atmosphere and Alkalinity and Dissolved Carbon to the Coastal Ocean: A Case Study From the Everglades National Park, Florida. J Geophys Res Biogeosci **125**. doi:10.1029/2020JG005812

Rodellas, V., T. C. Stieglitz, J. J. Tamborski, P. van Beek, A. Andrisoa, and P. G. Cook. 2021. Conceptual uncertainties in groundwater and porewater fluxes estimated by radon and radium mass balances. Limnol Oceanogr **66**: 1237–1255. doi:10.1002/lno.11678

Rosentreter, J. A., D. T. Maher, D. V. Erler, R. Murray, and B. D. Eyre. 2018. Seasonal and temporal CO2 dynamics in three tropical mangrove creeks – A revision of global mangrove CO2 emissions. Geochim Cosmochim Acta **222**: 729–745. doi:10.1016/j.gca.2017.11.026

Rosentreter, J. A., D. T. Maher, D. T. Ho, M. Call, J. G. Barr, and B. D. Eyre. 2017. Spatial and temporal variability of CO2 and CH4 gas transfer velocities and quantification of the CH4 microbubble flux in mangrove dominated estuaries. Limnol Oceanogr **62**: 561–578. doi:10.1002/lno.10444

Sadat-Noori, M., D. T. Maher, and I. R. Santos. 2016. Groundwater Discharge as a Source of Dissolved Carbon and Greenhouse Gases in a Subtropical Estuary. Estuaries and Coasts **39**: 639–656. doi:10.1007/s12237-015-0042-4

Saifullah, A. S. M., A. H. M. Kamal, M. H. Idris, A. H. Rajaee, and M. K. A. Bhuiyan. 2016. Phytoplankton in tropical mangrove estuaries: role and interdependency. Forest Sci Technol **12**: 104–113. doi:10.1080/21580103.2015.1077479

Santos, I. R., D. J. Burdige, T. C. Jennerjahn, and others. 2021. The renaissance of Odum's outwelling hypothesis in "Blue Carbon" science. Estuar Coast Shelf Sci **255**: 107361. doi:10.1016/j.ecss.2021.107361

Santos, I. R., D. T. Maher, and B. D. Eyre. 2012. Coupling automated radon and carbon dioxide measurements in coastal waters. Environ Sci Technol **46**: 7685–7691. doi:10.1021/es301961b

Santos, I. R., D. T. Maher, R. Larkin, J. R. Webb, and C. J. Sanders. 2019. Carbon outwelling and outgassing vs. burial in an estuarine tidal creek surrounded by mangrove and saltmarsh wetlands. Limnol Oceanogr **64**: 996–1013. doi:10.1002/lno.11090

Sippo, J. Z., D. T. Maher, D. R. Tait, C. Holloway, and I. R. Santos. 2016. Are mangroves drivers or buffers of coastal acidification? Insights from alkalinity and dissolved inorganic carbon export estimates across a latitudinal transect. Global Biogeochem Cycles **30**: 753–766. doi:10.1002/2015GB005324

Taillardat, P., P. Willemsen, C. Marchand, and others. 2018a. Assessing the contribution of porewater discharge in carbon export and CO2 evasion in a mangrove tidal creek (Can Gio, Vietnam). J Hydrol (Amst) **563**: 303–318. doi:10.1016/j.jhydrol.2018.05.042

Taillardat, P., A. D. Ziegler, D. A. Friess, D. Widory, V. Truong Van, F. David, N. Thành-Nho, and C. Marchand. 2018b. Carbon dynamics and inconstant porewater input in a mangrove tidal creek over contrasting seasons and tidal amplitudes. Geochim Cosmochim Acta **237**: 32–48. doi:10.1016/j.gca.2018.06.012

Tait, D. R., D. T. Maher, P. A. Macklin, and I. R. Santos. 2016. Mangrove pore water exchange across a latitudinal gradient. Geophys Res Lett **43**: 3334–3341. doi:10.1002/2016GL068289

Taniguchi, M., H. Dulai, K. M. Burnett, and others. 2019. Submarine Groundwater Discharge: Updates on Its Measurement Techniques, Geophysical Drivers, Magnitudes, and Effects. Front Environ Sci **7**: 1–26. doi:10.3389/fenvs.2019.00141

Vinh, T. Van, M. Allenbach, A. Joanne, and C. Marchand. 2019. Seasonal variability of CO2 fluxes at different interfaces and vertical CO2 concentration profiles within a Rhizophora mangrove forest (Can Gio, Viet Nam). Atmos Environ **201**: 301–309. doi:10.1016/j.atmosenv.2018.12.049

Wanninkhof, R. 2014. Relationship between wind speed and gas exchange over the ocean revisited. Limnol Oceanogr Methods **12**: 351–362. doi:10.4319/lom.2014.12.351

Weigel, V. F. 1978. Radon. Chemiker Zeitung **102**: 287–299.

Weiss, R. F. 1974. Carbon dioxide in water and seawater: the solubility of a non-ideal gas. Mar Chem **2**: 203–215. doi:10.1016/0304-4203(74)90015-2

Whitfield, A., and M. Elliott. 2011. Ecosystem and Biotic Classifications of Estuaries and Coasts, p. 99–124. *In* Treatise on Estuarine and Coastal Science. Elsevier.

Xiao, K., A. M. Wilson, H. Li, and others. 2021. Large CO2 release and tidal flushing in salt marsh crab burrows reduce the potential for blue carbon sequestration. Limnol Oceanogr **66**: 1–16. doi:10.1002/lno.11582

Zablocki, J. A., A. J. Andersson, and N. R. Bates. 2011. Diel Aquatic CO2 System Dynamics of a Bermudian Mangrove Environment. Aquat Geochem **17**: 841–859. doi:10.1007/s10498-011-9142-3

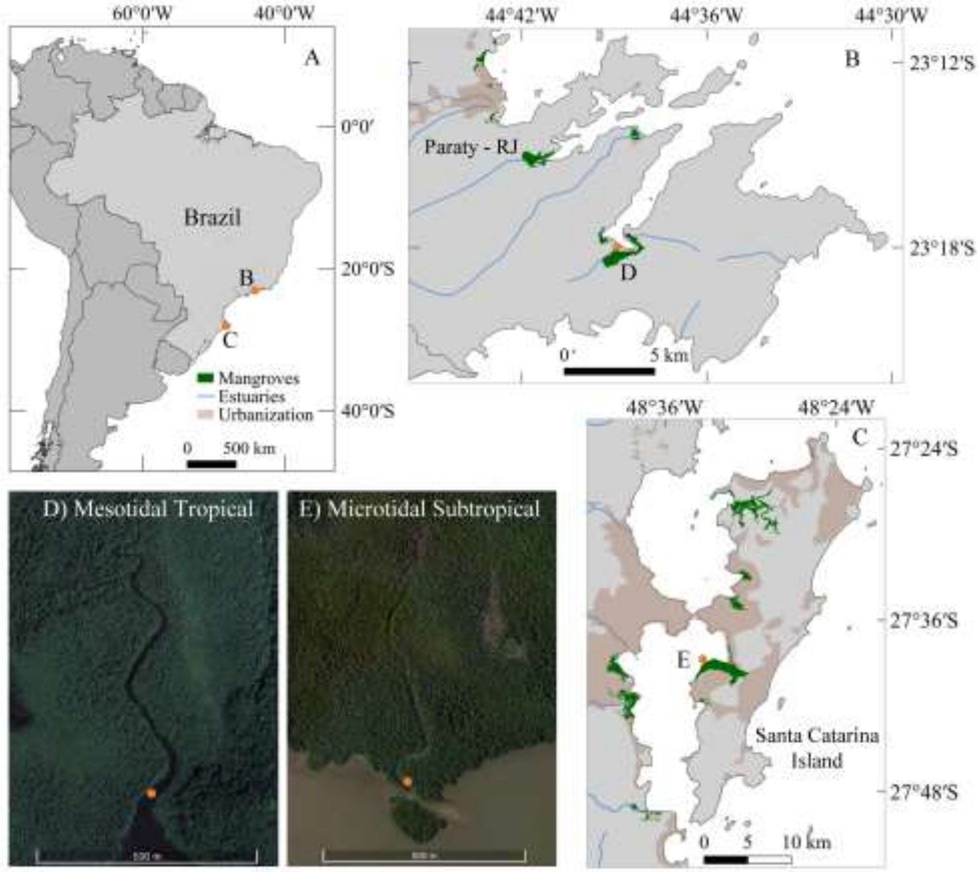

Figure 1. Location of the study sites in South America (A) and within regional settings (B & C). The locations of the orange dots (D & E) show the position where time-series observations were deployed. Porewaters were sampled in both sides of the tidal creeks around the orange dots.

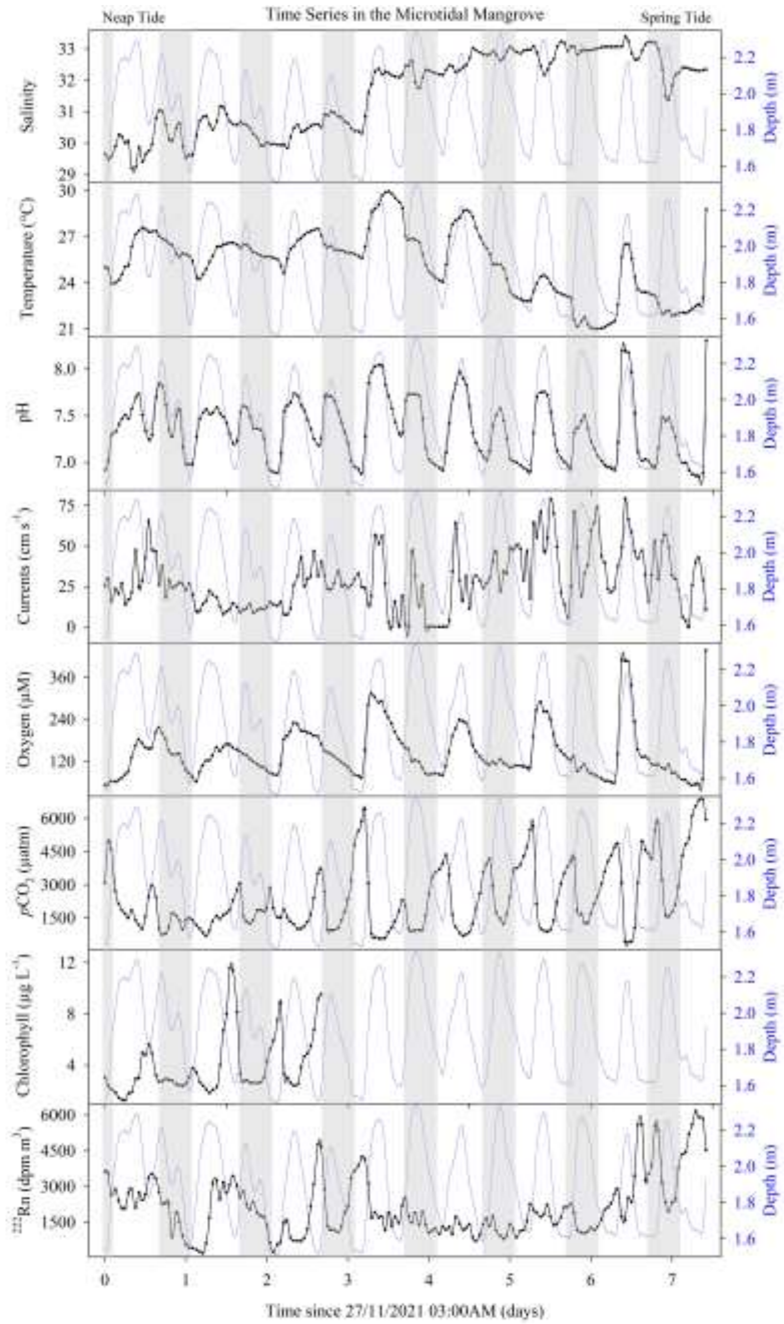

Figure 2. Time series observations of salinity, temperature, water currents, dissolved oxygen, pCO_2 and ^{222}Rn during a 7-days neap and spring tidal cycles in the microtidal mangrove. The white and shade bars represent day and night periods, respectively.

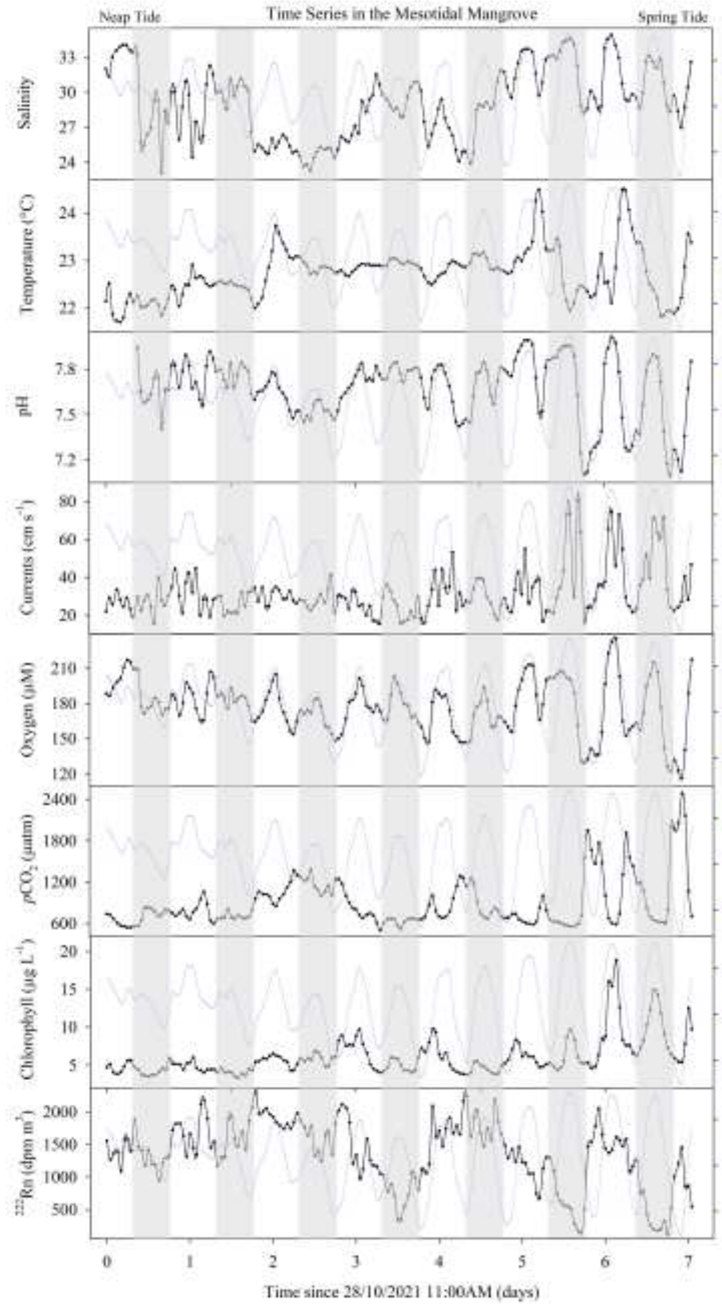

Figure 3. Time series observations of salinity, temperature, water currents, dissolved oxygen, pCO_2 and ^{222}Rn during a 7-days neap and spring tidal cycles in the mesotidal mangrove. The white and shade bars represent day and night periods, respectively.

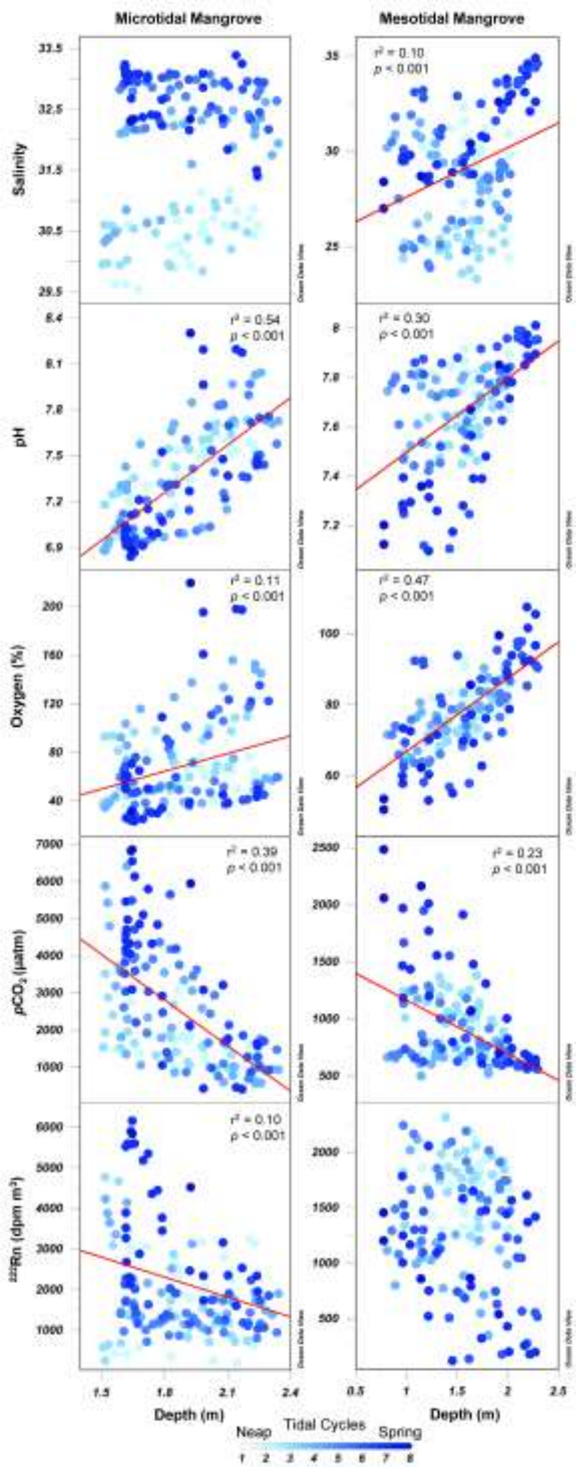

Figure 4. Linear regressions (r^2 and p-values) and scatterplots between depth and salinity, pH, oxygen saturation, pCO_2 and ^{222}Rn in both mangroves.

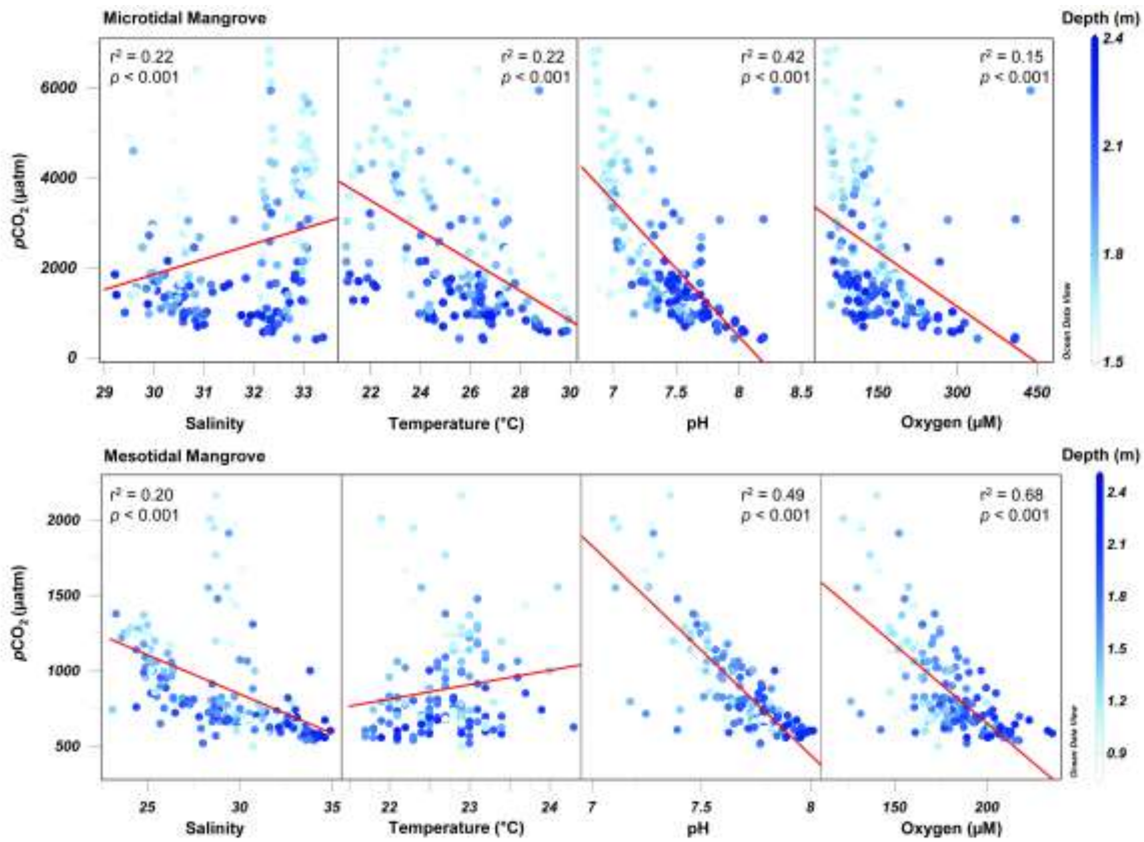

Figure 5. Linear regressions (r^2 and *p*-values) and scatterplots between pCO_2 and salinity, temperature, pH, and dissolved oxygen in both mangroves.

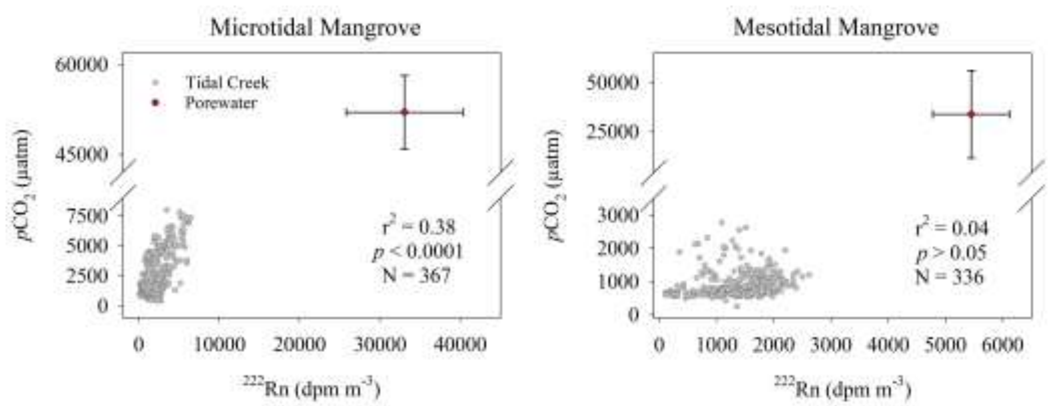

Figure 6. Correlation of pCO_2 with ^{222}Rn in both mangrove tidal creeks. Average of porewater samples concentrations is included for comparison (red circles with error bars).

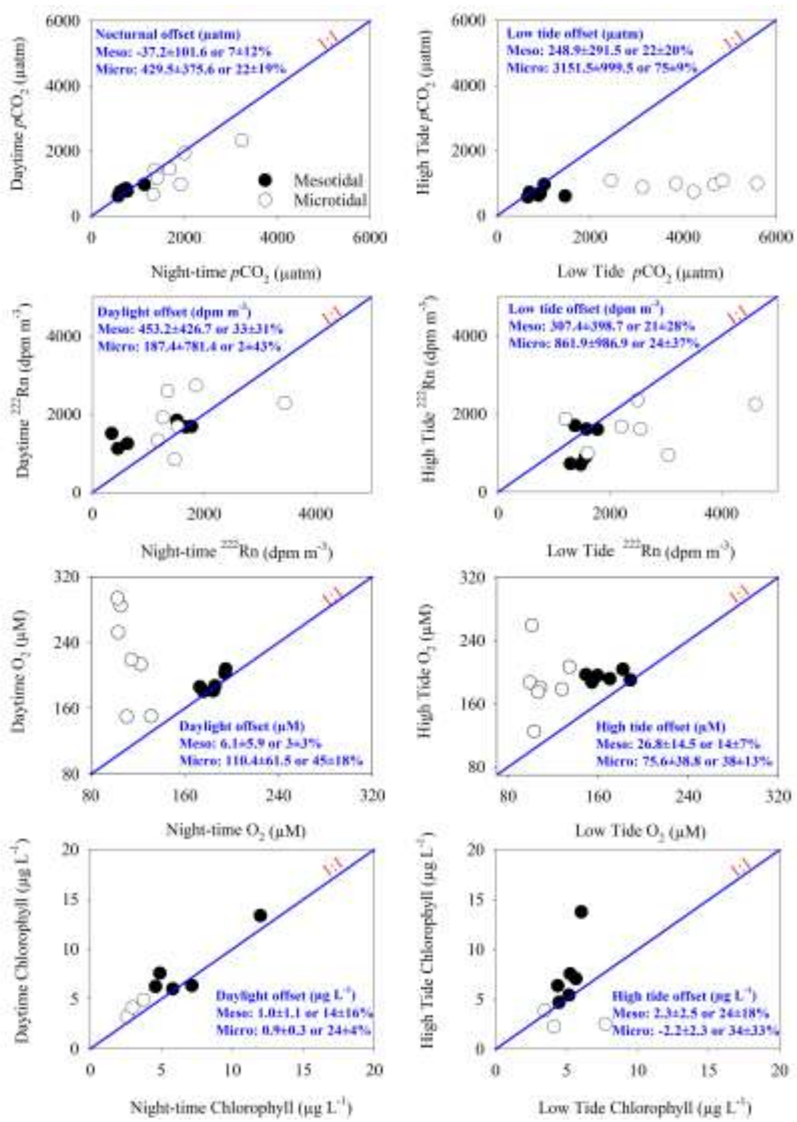

Figure 7. Distribution of pCO_2, dissolved oxygen, ^{222}Rn, and chlorophyll during diel (day/night) and tidal (low/high) cycles in both mangroves. Daytime and night-time were calculated from average concentrations using time intervals of 10am-3pm and 10pm-3am from each tidal cycle, respectively. High and low tide concentrations were calculated using the average of the two highest and lowest tides from each semidiurnal tidal cycle in the time-series. The blue 1:1 slope implies same values at low and high tides or during the day and night. Offsets were calculated as a percentage of deviation in relation to the conservative concentration (blue line) in each tidal or diel cycles.

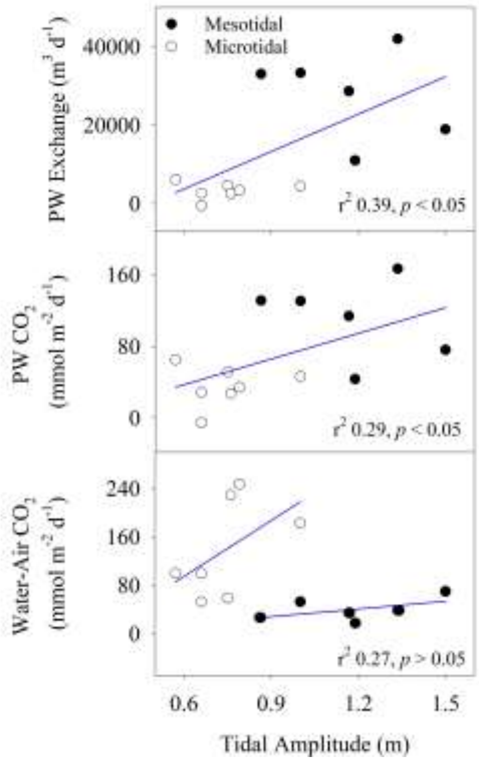

Figure 8. Linear regressions between tidal amplitudes and daily porewater (PW) exchange rates, porewater-delivered CO_2, and water-atmosphere CO_2 fluxes in both mangroves. Tidal amplitude was calculated by the difference between the highest and lowest depths during full daily tidal cycles.

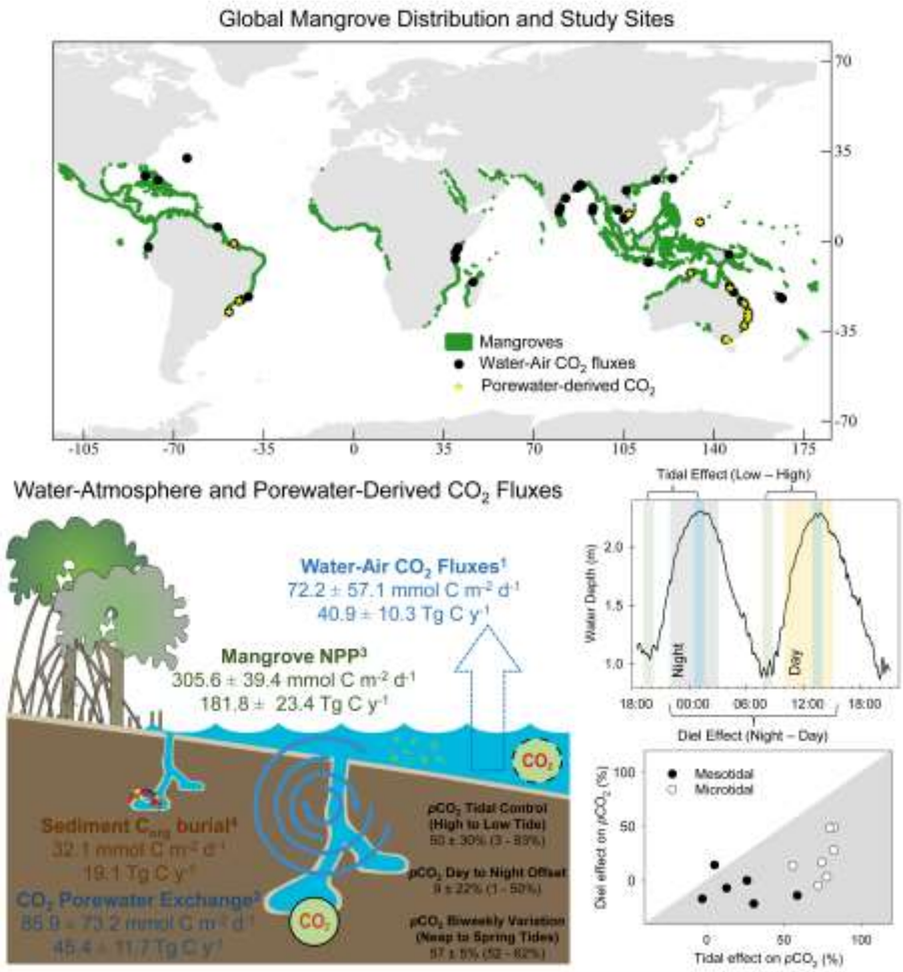

Figure 9. Conceptual model showing mangrove water-atmosphere[1] and porewater-derived[2] CO_2 global fluxes from table 5. Net primary production[3] (NPP) and sediment carbon burial[4] rates in mangroves are based on Alongi (2020) and Breithaupt and Steinmuller (2022), respectively. Results in m^2 of mangrove area were upscaled using total global mangrove area of 137759 Km^2 (Giri et al., 2011). Global datasets can be found in the supplementary material. Tidal, diel, and biweekly offsets represent the percentage deviation of pCO_2 between high/low tides, day/night and over neap/spring tidal cycles (Fig. 7). We used the lowest and highest daily water height to calculate the tidal offsets to enable comparations with a diel 24hrs cycle in the same time interval.

Table 1. Summary of variables of atmospheric and surface water parameters in both mangroves' tidal creeks during the time series observations. Average ± SD (minimum-maximum).

Parameter	Microtidal Subtropical	Mesotidal Tropical
Rainfall (mm)*	5.6	57.8
Air temperature (°C)	23.2 ± 2.6 (18.3 - 30.6)	21.8 ± 1.8 (18.2 - 26.5)
Wind speed (m s^{-1})	1.9 ± 1.2 (0.0 - 5.6)	1.2 ± 0.9 (0.0 - 3.9)
Current velocity (cm s^{-1})	28.6 ± 18.2 (0.1 - 79.3)	31.8 ± 12.8 (15.5 - 80.6)
Depth (m)	1.9 ± 0.3 (1.3 - 2.6)	1.6 ± 0.4 (0.6 - 2.3)
Tidal Range (m)	0.7 ± 0.1 (0.4 - 0.9)	1.3 ± 0.2 (0.9 - 1.8)
Salinity	31.6 ± 1.2 (29.2 - 33.4)	29.1 ± 3.0 (23.1 - 34.9)
Water temperature (°C)	25.3 ± 1.2 (21.0 - 29.9)	22.7 ± 0.5 (21.7 - 24.5)
pH	7.4 ± 0.3 (6.8 - 8.3)	7.7 ± 0.2 (7.1 - 8.0)
Oxygen (µM)	145.6 ± 72.8 (52.0 - 437.6)	177.3 ± 22.4 (116.3 - 235.2)
Oxygen (%)	69.2 ± 36.3 (23.3 - 219.5)	78.7 ± 10.8 (50.5 - 107.5)
Oxygen (mg L^{-1})	4.7 ± 2.3 (1.7 - 14.0)	5.7 ± 0.7 (3.7 - 7.5)
CO_2 (µM)	71.7 ± 47.9 (11.5 - 213.6)	28.3 ± 11.5 (15.6 - 80.6)
CO_2 (%)	582.1 ± 374.1 (99.1 - 1660.1)	216.3 ± 86.4 (121.0 - 601.6)
pCO_2 (µatm)	2403.9 ± 1545.0 (409.2 - 6856.3)	893.2 ± 357.0 (499.9 - 2484.6)
Chlorophyll (µg L^{-1})	3.9 ± 2.4 (1.2 - 11.6)	6.1 ± 2.5 (3.3 - 18.8)
^{222}Rn (dpm m^{-3})	2146.5 ± 1259.7 (203.0 - 6158.9)	1354.7 ± 508.7 (120.5 - 2315.5)

*Accumulated rainfall during the time series in both mangroves.

Table 2. Summary (average ± SD) of observations in porewater (endmember) for both mangroves.

Parameter	Microtidal	Mesotidal
Salinity	31.4 ± 0.7	24.4 ± 2.6
Temperature (°C)	22.4 ± 1.0	23.1 ± 0.6
pH	6.1 ± 0.1	6.8 ± 0.4
Oxygen (µM)	45.5 ± 44.0	N.D.
CO_2 (µM)	1631.1 ± 600.6	1052.9 ± 2266.8
pCO_2 (µatm)	52027.3 ± 20404.4	33792.4 ± 74083.2
^{222}Rn (dpm m^{-3})	33052.2 ± 7269.8	5449.0 ± 2218.4

Table 3. Water-atmosphere interface CO_2 fluxes (mmol m^{-2} d^{-1}) and gas transfer velocities (m d^{-1}) normalized to the Schmidt number (k_{600}) in the microtidal and mesotidal mangrove creeks based on the parameterization's models by B04 (Borges et al., 2004), H16 (Ho et al., 2016), R17 (Rosentreter et al., 2017), and J18 (Jeffrey et al., 2018). *Averages and standard deviations of all models combined during the time series (all data) in each mangrove and for the neap (first 2 days) and spring (last 2 days) tides separately.

	Microtidal Subtropical Mangrove			Mesotidal Tropical Mangrove		
	All data	Neap tide	Spring tide	All data	Neap tide	Spring tide
*CO_2	142.9 ± 140.7	90.4 ± 74.4	233.9 ± 161.7	38.4 ± 30.7	26.5 ± 12.1	56.1 ± 45.9
B04	160.0 ± 145.6	104.0 ± 74.6	247.4 ± 166.8	44.9 ± 41.4	30.9 ± 14.5	66.7 ± 65.7
H16	53.1 ± 50.7	34.3 ± 27.1	80.9 ± 56.3	15.5 ± 14.9	10.2 ± 4.8	23.4 ± 23.8
R17	132.6 ± 137.2	82.2 ± 71.2	223.0 ± 159.9	34.3 ± 25.5	23.9 ± 11.0	49.7 ± 36.7
J18	225.8 ± 237.1	141.3 ± 126.8	384.4 ± 279.5	59.0 ± 42.7	41.0 ± 18.7	84.5 ± 60.4
*k_{600}	2.6 ± 1.1	2.2 ± 0.8	3.0 ± 1.1	2.6 ± 0.8	2.4 ± 0.4	3.2 ± 1.0
B04	2.9 ± 1.0	2.6 ± 0.7	3.0 ± 0.7	2.9 ± 0.7	2.8 ± 0.5	3.4 ± 0.8
H16	1.0 ± 0.5	0.8 ± 0.3	1.0 ± 0.3	1.0 ± 0.3	0.9 ± 0.2	1.2 ± 0.3
R17	2.4 ±1.2	2.0 ± 0.8	3.0 ± 1.3	2.4 ± 0.9	2.2 ± 0.5	3.1 ± 1.2
J18	4.0 ± 2.1	3.4 ± 1.4	5.2 ± 2.3	4.2 ± 1.5	3.8 ± 0.8	5.3 ± 2.2

Table 4. Radon mass-balance, porewater exchange and CO_2 fluxes during the time series in both mangrove creeks. The missing radon source was assumed to be porewater exchange. dpm = decays per minute.

	Microtidal	**Mesotidal**
^{222}Rn budgets (10^7 dpm d^{-1})		
^{222}Rn flow (flood – ebb tides)	0.9 ± 5.7	1.4 ± 3.9
Atmospheric evasion	9.0 ± 2.8	9.1 ± 2.5
^{222}Rn decay	0.9 ± 0.4	0.8 ± 0.2
Sediment diffusion	0.3 ± 0.1	0.1 ± 0.1
^{222}Rn ingrowth from ^{226}Ra decay	0.3 ± 0.1	0.1 ± 0.1
Porewater flow (missing term)	10.2 ± 6.3	11.1 ± 3.9
Porewater exchange (10^3 m^3 d^{-1})	3.3 ± 2.1	27.8 ± 10.2
Mangrove catchment area (m^2)	146065	260112
Porewater exchange rate (cm d^{-1})	2.3 ± 1.4	10.7 ± 3.9
CO_2 porewater exchange (10^6 mmol d^{-1})	5.2 ± 3.3	28.7 ± 10.5
CO_2 porewater exchange rate (mmol m^2 d^{-1})	35.5 ± 22.5	110.4 ± 40.2
CO_2 water-air fluxes (mmol m^2 d^{-1})	142.9 ± 140.7	38.4 ± 30.7

Table 5. Global CO_2 exports by porewater exchange and water-atmosphere fluxes in mangroves. Mangrove areas on micro-, meso- and macrotidal systems were retrieved from Giri et al. (2011) and Call at al. (2019). Global datasets were compilated to upscale average porewater-derived (Tab. S1, N = 16) and water-atmosphere (Tab. S2, N = 52) CO_2 fluxes by tidal ranges and global mangroves.

Tidal Range	**Global Area (Km^2)**	**Porewater-exchange (cm d^{-1})**	**Porewater-derived CO_2 (mmol C m^{-2} d^{-1})**	**Porewater-derived CO_2 (Tg C y^{-1})**	**Water-Air CO_2 (mmol C m^{-2} d^{-1})**	**Water-Air CO_2 (Tg C y^{-1})**
Microtidal (< 1.5 m)	27967	10.1±6.7	94.2±68.5	11.4±8.3	82.0±60.8	9.9±7.3
Mesotidal (1.6 - 4 m)	70935	12.3±11.3	91.6±84.0	28.1±25.7	53.7±40.9	16.4±12.5
Macrotidal (> 4 m)	38857	3.4±1.5	35.3±5.9	5.9±1.1	87.3±68.0	14.5±10.9
Global Mangroves	137760	10.1±8.9	85.9±73.2	45.4±11.7	72.2±57.1	40.9±10.3

Appendix A. Supplementary Material

Table A1. Global compilation of porewater exchange rates, pCO_2 in porewater and porewater-derived CO_2 exchange in mangroves. Table updated from Chen et al. (2021).

Mangrove area	Latitude	Longitude	Country	Tidal range (m)	Porewater exchange (cm d^{-1})	pCO_2 in porewater (μatm)	Porewater-derived CO_2 (mmol m^{-2} d^{-1})	References
Americas								
Florianopolis	-27.65	-48.55	Brazil	0.9	2.3±1.4	52027±20404	35.5±22.5	This Study
Amazon	-0.87	-46.65	Brazil	5.3	1.9±1.9	29459±24076	41.2±37.2	(Call et al. 2019b; Cabral et al. 2021)
Paraty	-23.30	-44.65	Brazil	1.7	10.7±3.9	33792±74083	110.4±40.2	This Study
Asia								
Can Gio	10.51	106.88	Vietnam	2.9	4.9±1.5	18796±13820	26	(Taillardat et al. 2018a; b)
Oceania								
Darwin	-12.44	130.87	Australia	5.4	4.9	82717±25214	29.4±13.1	(Tait et al. 2016; Sippo et al. 2016)
Badeldaob 1	7.37	134.58	Palau	1.1	3.3±3.3	29000±33000	31.0	(Call et al. 2019a)
Badeldaob 2	7.39	134.59	Palau	1.1	6.2±4.8	27600±46200	72	(Call et al. 2019a)
Barwon	-38.26	144.50	Australia	1.7	4.9	16179±7228	29.4±13.1	(Tait et al. 2016; Sippo et al. 2016)
Western Port	-38.23	145.26	Australia	1.4	6.7-27	237-5329	14	(Faber et al. 2014)
Hinch	-18.26	146.26	Australia	2.1	35.5	23634±10545	254.2±112.1	(Tait et al. 2016; Sippo et al. 2016)
Newcastle	-32.85	151.77	Australia	0.9	14.7	48183±14743	233.0±72.8	(Tait et al. 2016; Sippo et al. 2016)
1770	-24.19	151.87	Australia	2.9	2.1	16605±9408	10.3±6.3	(Tait et al. 2016; Sippo et al. 2016)
Coffs Creek estuary	-30.30	153.13	Australia	0.5	23.0±6.7	3170-70700	136.0	(Chen et al. 2021)
Jacobs	-27.78	153.38	Australia	2.2	15.9	24055±9801	119.5±49.0	(Tait et al. 2016; Sippo et al. 2016)
Moreton Bay	-27.78	153.40	Australia	1.2	15.9	9510-42500	119.0	(Call et al. 2015; Tait et al. 2016)
Evans Head	-29.12	153.43	Australia	1.1	9.0±5.1	69798±4513	120.0±78.0	(Santos et al. 2019)

Table A2. Tidal amplitude, water pCO_2 (range) and average water-atmosphere CO_2 flux from this study and previously published data in 50 mangrove systems worldwide. Table updated from earlier global compilations (Borges et al. 2003; Call et al. 2015; Rosentreter et al. 2018).

Mangrove area	Latitude	Longitude	Country	Tidal range (m)	pCO_2 (μatm)	CO_2 flux (mmol m^{-2} d^{-1})	Reference
Americas							
Shark River	25.3633	-81.0773	USA	1.98	975–6,016	102.0	(Ho et al. 2016)
Guayas river	-2.4313	-79.9087	Ecuador	4.00	1,200–5,100	248.9	(Belliard et al. 2022)
Norman's Pond	23.7739	-76.1268	Bahamas	1.20	395–690	13.8	(Borges et al. 2003)
Mangrove bay	32.3038	-64.8651	Bermuda	0.60	268–4,823	65.0	(Zablocki et al. 2011)
Sinnamary estuary	5.4531	-53.0131	French Guiana	3.20	391–7,216	157.0	(Ray et al. 2020)
Florianópolis	-27.6500	-48.5500	Brazil	0.80	499.9–2485	142.9	This Study
Amazon	-0.8741	-46.6506	Brazil	4.75	592–15,361	174.0	(Call et al. 2019b)
Paraty	-23.3000	-44.6500	Brazil	1.70	409.2–6,856	38.1	This Study
Itacuracá Creek	-22.9341	-43.8934	Brazil	1.20	660–7,700	113.5	(Ovalle et al. 1990)
Paraíba do Sul	-21.6054	-41.0520	Brazil	0.70	456–22,000	134.8	(Cotovicz et al. 2020)
Africa							
Mtoni	-6.8733	39.4630	Tanzania	3.00	400–1,700	18.0	(Kristensen et al. 2008)
Ras Dege	-6.8733	39.4630	Tanzania	2.60	400–5,050	33.7	(Bouillon et al. 2007c)
Kidogoweni (Gazi bay)	-4.4087	39.5133	Kenya	3.00	1,480–6,435	71.0	(Bouillon et al. 2007b)
Kinondo creek (Gazi bay)	-4.0021	39.6466	Kenya	3.00	575–6,435	52.0	(Bouillon et al. 2007b)
Tana River Delta	-2.5356	40.5306	Kenya	4.00	230–5,300	58.0	(Bouillon et al. 2007a)
Betsiboka	-15.8850	46.3400	Madagascar	3.50	270–1,530	9.1	(Ralison et al. 2008)
Asia							
Cauvery Delta	11.3978	79.8080	India	1.00	654–4,102	51.9	(Ramesh et al. 2007)
Adyar Estuary	13.0131	80.2734	India	1.00	437–7,978	48.7	(Ramesh et al. 2007)
Gautami Godavari Estuary	16.7419	82.3355	India	2.00	430–4,770	43.4	(Bouillon et al. 2003; Borges et al. 2003; Ramesh et al. 2007)
Dhamra Estuary	20.7739	86.9470	India	4.50	422–3,869	65.0	(Akhand et al. 2022)
Hooghly Estuary	22.0049	88.0590	India	7.00	559–3,679	94.3	(Akhand et al. 2022)
Mooriganga Estuary	21.6961	88.3940	India	5.94	152–1,530	7.7	(Borges et al. 2003)
Saptamukhi Estuary	21.7355	88.4992	India	5.10	193–4,000	28.5	(Borges et al. 2003; Biswas et al. 2004)

Thakuran Estuary	21.7047	88.5239	India	5.50	160–737	0.3	(Biswas et al. 2004; Akhand et al. 2013)
Malta Estuary	21.7671	88.5623	India	7.00	429–1,760	31.0	(Akhand et al. 2022)
Wright Myo	11.7013	92.6964	Andaman Islands	1.90	1,246–7,703	61.1	(Ramesh et al. 2007; Linto et al. 2014)
Kalighat	13.0626	92.9378	Andaman Islands	1.90	1,574–7,888	70.8	(Ramesh et al. 2007; Linto et al. 2014)
Trat	12.2068	102.5653	Thailand	3.00	1650.00	18.9	(Ikeda 2007)
Kiên Vàng	8.6074	105.0111	Vietnam	0.80	704–8,136	93.5	(Koné and Borges 2008)
Ca Mau	8.7806	105.1883	Vietnam	0.80	700-1,400	54.2	(Koné and Borges 2008)
Tam Giang	8.8168	105.2166	Vietnam	0.80	767–11,481	135.0	(Koné and Borges 2008)
Nam Ma River, Thanh Hóa	19.7734	105.8741	Thailand	4.00	1092.00	33.0	(Ikeda 2007)
Can Gio	10.5057	106.8824	Vietnam	3.20	1,088–17,767	142.0	(Taillardat et al. 2018a)
Gilimanuk Bay	-8.1670	114.4687	Indonesia	1.30	700–2,101	18.1	(Macklin et al. 2019)
Yunxiao Creek	23.9274	117.4240	China	4.67	928–8,000	79.2	(Lu et al. 2023)
Iriomote Island	24.3841	123.8863	Japan	1.00	401–2,667	24.0	(Akhand et al. 2021)
Oceania							
Darwin	-12.4400	130.8700	Australia	5.40	622–1,263	40.0	(Sippo et al. 2016)
Badeldaob	7.3911	134.5856	Palau	1.10	484–4,752	57.5	(Call et al. 2019a)
Barwon Head	-38.2600	144.5000	Australia	1.70	415–827	9.0	(Sippo et al. 2016)
Nagada Creek	-5.1544	145.7924	Papua New Guinea	1.00	540–1,680	43.6	(Borges et al. 2003)
Johnstone Estuary	-17.5090	146.0660	Australia	1.60	387–9,744	110.6	(Rosentreter et al. 2018)
Hinchinbrook Island	-18.2600	146.2600	Australia	2.10	1,341–3,304	30.0	(Sippo et al. 2016)
Burdekin Estuary	-19.6870	147.6110	Australia	1.50	617–13,031	221.0	(Rosentreter et al. 2018)
Fitzroy Estuary	-23.5230	150.8700	Australia	3.70	699–7,947	139.2	(Rosentreter et al. 2018)
Newcastle	-32.8500	151.7700	Australia	0.90	404–3,224	46.0	(Sippo et al. 2016)
Seventeen Seventy	-24.1900	151.8700	Australia	2.90	314–1,399	10.0	(Sippo et al. 2016)
Coffs Creek estuary	-30.3019	153.1298	Australia	0.51	403–7,920	49.0	(Jeffrey et al. 2018)
Jacobs Well	-27.7800	153.4000	Australia	1.50	531–5,036	19.0	(Sippo et al. 2016)
Moreton Bay	-27.7691	153.4110	Australia	1.53	385–26,106	201.6	(Call et al. 2015)
Evans Head	-29.1200	153.4300	Australia	1.10	400–2,500	85.3	(Santos et al. 2019)
La Foa Estuary	-21.7320	165.7563	New Caledonia	2.00	537–4,023	78.6	(Leopold et al. 2017)

Ouemo	-22.2806	166.4711	New Caledonia	1.70	NA	80.4	(Jacotot et al. 2018)

References

Akhand, A., A. Chanda, S. Dutta, S. Manna, P. Sanyal, S. Hazra, K. H. Rao, and V. K. Dadhwal. 2013. Dual character of Sundarban estuary as a source and sink of CO2 during summer: An investigation of spatial dynamics. Environ Monit Assess **185**: 6505–6515. doi:10.1007/s10661-012-3042-x

Akhand, A., A. Chanda, K. Watanabe, S. Das, T. Tokoro, S. Hazra, and T. Kuwae. 2022. Drivers of inorganic carbon dynamics and air–water CO2 fluxes in two large tropical estuaries: Insights from coupled radon (222Rn) and pCO2 surveys. Limnol Oceanogr **67**: S118–S132. doi:10.1002/lno.12075

Akhand, A., K. Watanabe, A. Chanda, and others. 2021. Lateral carbon fluxes and CO2 evasion from a subtropical mangrove-seagrass-coral continuum. Science of the Total Environment **752**: 142190. doi:10.1016/j.scitotenv.2020.142190

Belliard, J. P., S. Hernandez, S. Temmerman, and others. 2022. Carbon dynamics and CO2 and CH4 exchange in the mangrove dominated Guayas river delta, Ecuador. Estuar Coast Shelf Sci **267**. doi:10.1016/j.ecss.2022.107766

Biswas, H., S. K. Mukhopadhyay, T. K. De, S. Sen, and T. K. Jana. 2004. Biogenic controls on the air-water carbon dioxide exchange in the Sundarban mangrove environment, northeast coast of Bay of Bengal, India. Limnol Oceanogr **49**: 95–101. doi:10.4319/lo.2004.49.1.0095

Borges, A. v., S. Djenidi, G. Lacroix, J. Théate, B. Delille, and M. Frankignoulle. 2003. Atmospheric CO2 flux from mangrove surrounding waters. Geophys Res Lett **30**. doi:10.1029/2003GL017143

Bouillon, S., F. Dehairs, L.-S. Schiettecatte, and A. V. Borges. 2007a. Biogeochemistry of the Tana estuary and delta (northern Kenya). Limnol Oceanogr **52**: 46–59. doi:10.4319/lo.2007.52.1.0046

Bouillon, S., F. Dehairs, B. Velimirov, G. Abril, and A. V. Borges. 2007b. Dynamics of organic and inorganic carbon across contiguous mangrove and seagrass systems (Gazi Bay, Kenya). J Geophys Res **112**: G02018. doi:10.1029/2006JG000325

Bouillon, S., M. Frankignoulle, F. Dehairs, B. Velimirov, A. Eiler, G. Abril, H. Etcheber, and A. V. Borges. 2003. Inorganic and organic carbon biogeochemistry in the Gautami Godavari estuary (Andhra Pradesh, India) during pre-monsoon: The local impact of extensive mangrove forests. Global Biogeochem Cycles **17**. doi:10.1029/2002gb002026

Bouillon, S., J. J. Middelburg, F. Dehairs, A. v. Borges, G. Abril, M. R. Flindt, S. Ulomi, and E. Kristensen. 2007c. Importance of intertidal sediment processes and porewater exchange on the water column biogeochemistry in a pristine mangrove creek (Ras Dege, Tanzania). Biogeosciences **4**: 311–322. doi:10.5194/bg-4-311-2007

Cabral, A., T. Dittmar, M. Call, and others. 2021. Carbon and alkalinity outwelling across the groundwater-creek-shelf continuum off Amazonian mangroves. Limnol Oceanogr Lett **6**: 369–378. doi:10.1002/lol2.10210

Call, M., D. T. Maher, I. R. Santos, and others. 2015. Spatial and temporal variability of carbon dioxide and methane fluxes over semi-diurnal and spring-neap-spring timescales in a mangrove creek. Geochim Cosmochim Acta **150**: 211–225. doi:10.1016/j.gca.2014.11.023

Call, M., C. J. Sanders, P. A. Macklin, I. R. Santos, and D. T. Maher. 2019a. Carbon outwelling and emissions from two contrasting mangrove creeks during the monsoon storm season in Palau, Micronesia. Estuar Coast Shelf Sci **218**: 340–348. doi:10.1016/j.ecss.2019.01.002

Call, M., I. R. Santos, T. Dittmar, C. E. de Rezende, N. E. Asp, and D. T. Maher. 2019b. High pore-water derived CO 2 and CH 4 emissions from a macro-tidal mangrove creek in the Amazon region. Geochim Cosmochim Acta **247**: 106–120. doi:10.1016/j.gca.2018.12.029

Chen, X., I. R. Santos, M. Call, and others. 2021. The mangrove CO2 pump: Tidally driven pore-water exchange. Limnol Oceanogr **66**: 1563–1577. doi:10.1002/lno.11704

Cotovicz, L. C., L. O. Vidal, C. E. de Rezende, and others. 2020. Carbon dioxide sources and sinks in the delta of the Paraíba do Sul River (Southeastern Brazil) modulated by carbonate thermodynamics, gas exchange and ecosystem metabolism during estuarine mixin. Mar Chem **226**: 103869. doi:10.1016/j.marchem.2020.103869

Faber, P. A., V. Evrard, R. J. Woodland, I. C. Cartwright, and P. L. M. Cook. 2014. Pore-water exchange driven by tidal pumping causes alkalinity export in two intertidal inlets. Limnol Oceanogr **59**: 1749–1763. doi:10.4319/lo.2014.59.5.1749

Ho, D. T., N. Coffineau, B. Hickman, N. Chow, T. Koffman, and P. Schlosser. 2016. Influence of current velocity and wind speed on air-water gas exchange in a mangrove estuary. Geophys Res Lett **43**: 3813–3821. doi:10.1002/2016GL068727

Ikeda, Y. 2007. Carbon dynamics in Japan, Thailand and Vietnam mangrove waters. Greenhouse Gas and Carbon Balances in Mangrove Coastal Ecosystems (eds. Y. Tateda, RC Upstill-Goddard, T. Goreau, D. Alongi, E. Kristensen and G. Wattayakorn) 51–60.

Jacotot, A., C. Marchand, and M. Allenbach. 2018. Tidal variability of CO2 and CH4 emissions from the water column within a Rhizophora mangrove forest (New Caledonia). Science of the Total Environment **631–632**: 334–340. doi:10.1016/j.scitotenv.2018.03.006

Jeffrey, L. C., D. T. Maher, I. R. Santos, M. Call, M. J. Reading, C. Holloway, and D. R. Tait. 2018. The spatial and temporal drivers of pCO2, pCH4 and gas transfer velocity within a subtropical estuary. Estuar Coast Shelf Sci **208**: 83–95. doi:10.1016/j.ecss.2018.04.022

Koné, Y. J. M., and A. v. Borges. 2008. Dissolved inorganic carbon dynamics in the waters surrounding forested mangroves of the Ca Mau Province (Vietnam). Estuar Coast Shelf Sci **77**: 409–421. doi:10.1016/j.ecss.2007.10.001

Kristensen, E., M. R. Flindt, S. Ulomi, A. v. Borges, G. Abril, and S. Bouillon. 2008. Emission of CO2 and CH4 to the atmosphere by sediments and open waters in two Tanzanian mangrove forests. Mar Ecol Prog Ser **370**: 53–67. doi:10.3354/meps07642

Leopold, A., C. Marchand, J. Deborde, and M. Allenbach. 2017. Water Biogeochemistry of a Mangrove-Dominated Estuary Under a Semi-Arid Climate (New Caledonia). Estuaries and Coasts **40**: 773–791. doi:10.1007/s12237-016-0179-9

Linto, N., J. Barnes, R. Ramachandran, J. Divia, P. Ramachandran, and R. C. Upstill-Goddard. 2014. Carbon Dioxide and Methane Emissions from Mangrove-Associated Waters of the Andaman Islands, Bay of Bengal. Estuaries and Coasts **37**: 381–398. doi:10.1007/s12237-013-9674-4

Lu, Z., F. Wang, K. Xiao, Y. Wang, Q. Yu, P. Cheng, and N. Chen. 2023. Carbon dynamics and greenhouse gas outgassing in an estuarine mangrove wetland with high input of riverine nitrogen. Biogeochemistry **162**: 221–235. doi:10.1007/s10533-022-00999-5

Macklin, P. A., I. G. N. A. Suryaputra, D. T. Maher, D. Murdiyarso, and I. R. Santos. 2019. Drivers of CO2 along a mangrove-seagrass transect in a tropical bay: Delayed groundwater seepage and seagrass uptake. Cont Shelf Res **172**: 57–67. doi:10.1016/j.csr.2018.10.008

Ovalle, A. R. C., C. E. Rezende, L. D. Lacerda, and C. A. R. Silva. 1990. Factors Affecting the Hydrochemistry of a Mangrove Tidal Creek, Sepetiba Bay, Brazil.

Ralison, O. H., A. V. Borges, F. Dehairs, J. J. Middelburg, and S. Bouillon. 2008. Carbon biogeochemistry of the Betsiboka estuary (north-western Madagascar). Org Geochem **39**: 1649–1658. doi:10.1016/j.orggeochem.2008.01.010

Ramesh, R., R. Purvaja, V. Neetha, J. Divia, J. Barnes, and R. C. Upstill-Goddard. 2007. CO2 and CH4 emissions from Indian mangroves and surrounding waters. Greenhouse Gas and Carbon Balances in Mangrove Coastal Ecosystems.

Ray, R., G. Thouzeau, R. Walcker, V. Vantrepotte, G. Gleixner, S. Morvan, J. Devesa, and E. Michaud. 2020. Mangrove-Derived Organic and Inorganic Carbon Exchanges Between the Sinnamary Estuarine System (French Guiana, South America) and Atlantic Ocean. J Geophys Res Biogeosci **125**. doi:10.1029/2020JG005739

Rosentreter, J. A., D. T. Maher, D. v. Erler, R. Murray, and B. D. Eyre. 2018. Seasonal and temporal CO2 dynamics in three tropical mangrove creeks – A revision of global mangrove CO2 emissions. Geochim Cosmochim Acta **222**: 729–745. doi:10.1016/j.gca.2017.11.026

Santos, I. R., D. T. Maher, R. Larkin, J. R. Webb, and C. J. Sanders. 2019. Carbon outwelling and outgassing vs. burial in an estuarine tidal creek surrounded by mangrove and saltmarsh wetlands. Limnol Oceanogr **64**: 996–1013. doi:10.1002/lno.11090

Sippo, J. Z., D. T. Maher, D. R. Tait, C. Holloway, and I. R. Santos. 2016. Are mangroves drivers or buffers of coastal acidification? Insights from alkalinity and dissolved inorganic carbon export estimates across a latitudinal transect. Global Biogeochem Cycles **30**: 753–766. doi:10.1002/2015GB005324

Taillardat, P., P. Willemsen, C. Marchand, and others. 2018a. Assessing the contribution of porewater discharge in carbon export and CO2 evasion in a mangrove tidal creek (Can Gio, Vietnam). J Hydrol (Amst) **563**: 303–318. doi:10.1016/j.jhydrol.2018.05.042

Taillardat, P., A. D. Ziegler, D. A. Friess, D. Widory, V. Truong Van, F. David, N. Thành-Nho, and C. Marchand. 2018b. Carbon dynamics and inconstant porewater input in a mangrove tidal creek over contrasting seasons and tidal amplitudes. Geochim Cosmochim Acta **237**: 32–48. doi:10.1016/j.gca.2018.06.012

Tait, D. R., D. T. Maher, P. A. Macklin, and I. R. Santos. 2016. Mangrove pore water exchange across a latitudinal gradient. Geophys Res Lett **43**: 3334–3341. doi:10.1002/2016GL068289

Zablocki, J. A., A. J. Andersson, and N. R. Bates. 2011. Diel Aquatic CO2 System Dynamics of a Bermudian Mangrove Environment. Aquat Geochem **17**: 841–859. doi:10.1007/s10498-011-9142-3